Draft version June 19, 2014
Preprint typeset using LaTeX style emulateapj v. 5/2/11

arXiv:1406.4774v1 [astro-ph.HE] 18 Jun 2014

NON-THERMAL GAMMA-RAY EMISSION FROM DELAYED PAIR BREAKDOWN IN A MAGNETIZED AND PHOTON-RICH OUTFLOW

Ramandeep Gill and Christopher Thompson
Canadian Institute for Theoretical Astrophysics, 60 St. George St., Toronto, ON M5S 3H8, Canada
Draft version June 19, 2014

ABSTRACT

We consider delayed, volumetric heating in a magnetized outflow that has broken out of a confining medium and expanded to a high Lorentz factor ($\Gamma \sim 10^2 - 10^3$) and low optical depth to scattering ($\tau_{\rm T} \sim 10^{-3} - 10^{-2}$). The energy flux at breakout is dominated by the magnetic field, with a modest contribution from quasi-thermal gamma rays whose spectrum was calculated in Paper I. We focus on the case of extreme baryon depletion in the magnetized material, but allow for a separate baryonic component that is entrained from a confining medium. Dissipation is driven by relativistic motion between these two components, which develops once the photon compactness drops below $4 \times 10^3 (Y_e/0.5)^{-1}$. We first calculate the acceleration of the magnetized component following breakout, showing that embedded MHD turbulence provides significant inertia, the neglect of which leads to unrealistically high estimates of flow Lorentz factor. After re-heating begins, the pair and photon distributions are evolved self-consistently using a one-zone kinetic code that incorporates an exact treatment of Compton scattering, pair production and annihilation, and Coulomb scattering. Heating leads to a surge in pair creation, and the scattering depth saturates at $\tau_{\rm T} \sim$ 1-4. The plasma maintains a very low ratio of particle to magnetic pressure, and can support strong anisotropy in the charged particle distribution, with cooling dominated by Compton scattering. High-energy power-law spectra with photon indices in the range observed in GRBs ($-3 < \beta < -3/2$) are obtained by varying the ratio of heat input to the seed energy in quasi-thermal photons. We contrast our results with those for continuous heating across an expanding photosphere, and show that the latter model produces soft-hard evolution that is inconsistent with observations of GRBs.
Subject headings: MHD — plasmas — radiative transfer — scattering — gamma rays: bursts

1. INTRODUCTION

Most gamma-ray bursts (GRBs) appear to mark the birth of stellar-mass black holes (Paczynski 1986; Eichler et al. 1989; Woosley 1993). A magnetized jet extracting energy from a black hole ergosphere (Blandford & Znajek 1977) is strongly depleted in baryons, but the jet must propagate through a dense, confining medium. As a result, the jet carries an intense thermal radiation field as well as a magnetic field.

The central thesis of this paper is that non-thermal gamma-ray emission results from the interaction between the thermal radiation field and a time-dependent magnetic field (Thompson 1994, 2006; Mészáros & Rees 1997; Spruit et al. 2001; Giannios 2006). Our focus is on the dynamics and dissipation of the jet after breakout, with a goal of accounting for the high-energy spectra of GRBs, and basic features of their pulse behavior.

A major part of the problem involves understanding where dissipation is concentrated. This is a significant theoretical challenge, given that the jet maintains a very high energy density and compactness over eight to ten decades in radius outward from the engine. Our approach is to divide the GRB emission process into two major components: dissipation before breakout, while the jet Lorentz factor is still relatively low; and a second phase of dissipation that is delayed to a large radius and – importantly – to a low scattering depth.

This means that a magnetized GRB outflow characteristically develops *two* pair-dominated photospheres. The radiation field advected by the jet is rich in electron-positron pairs close to the engine (Goodman 1986; Shemi & Piran 1990), and a moderately large scattering depth in pairs can be maintained by continued heating out to a considerable distance from the engine. When most of the jet energy flux is carried by the magnetic field at breakout, relaxation to thermal equilibrium results in a flat spectrum below the spectral peak, as is observed in GRBs (Thompson & Gill 2014a, hereafter Paper I). The spectral peak also sits in the observed range when the Lorentz factor inside breakout remains modest, $\Gamma \sim 1/\theta$. Softer spectral peaks (which may correspond to X-ray flashes) result from jets whose photospheres are dominated by electrons and ions (Paper I).

A rapid transition to transparency after breakout allows the magnetofluid to accelerate outward, by a combination of radiation pressure and the Lorentz force (Russo & Thompson 2013a,b); and helps to preserve a narrow peak in the spectrum.

Although the pairs can remain sub-relativistic during the first heating phase, they become relativistic enough to upscatter thermal photons above the pair-creation threshold during the second heating phase. The resulting surge in pair creation leads to a drop in mean particle energy while heating continues.

We find that a broad, non-thermal, Comptonized spectrum is created. There is a smooth connection to the thermal peak above a seed radiation compactness $\ell_{\rm th} \sim 300$ and total compactness, including heat input, $\ell_{\rm tot} \sim 10^3$. The required heating is spatially distributed, and can easily be supplied by the damping of hydromagnetic turbulence. This particular mechanism re-

sults in longitudinal heating of the embedded pairs along the background magnetic field, with an enhancement of Compton emission over synchrotron (Thompson & Blaes 1998; Thompson 2006). In contrast with the approach taken by Ghisellini & Celotti (1999), Giannios (2006) and Lazzati & Begelman (2010), the high-energy spectrum is mainly the result of single scatterings of thermal photons by a gradually softening relativistic particle population, not of multiple scattering by trans-relativistic pairs.

The thermal radiation field also plays a more central role in the outflow dynamics and emission than it does in the approach taken by Usov (1994) and Lyutikov & Blandford (2003) to strongly magnetized outflows. Those authors assume that fireball radiation decouples early on from the magnetic field (forming, e.g. a soft thermal precursor), leaving frozen-in electrons and pairs that emit synchrotron radiation after re-heating.

Regarding the trigger for delayed dissipation, we focus on the baryons that are embedded in the magnetized jet during breakout from the confining medium. Some residual baryons are pulled outward by the hyper-Eddington radiation flux, and decouple at a large radius where the jet compactness drops below a well-defined level. The magnetic field then is strongly distorted by the differential motion of the baryons, which supplies enough energy to account for the non-thermal tails of GRBs. The draining of baryons from the jet head also limits the Lorentz factor to $\Gamma \sim 1/\theta$ at breakout.

Magnetic reconnection remains a natural possibility in a magnetized jet, but pinning down where it operates depends on understanding the time evolution of a dynamo process in the engine. The simplest version of a magnetically striped wind (Drenkhahn & Spruit 2002), which is based on force-free models of pulsars, is inconsistent with a black-hole driven jet. A similiar difficulty arises in localizing the activity of internal shocks.

1.1. *Plan of the Paper*

After some further introduction to the problem of GRB prompt emission, in Section 3 we revisit the acceleration of a hot, magnetized jet that has become transparent to scattering. We take into account the inertia provided by MHD turbulence that is frozen into the expanding jet, which easily dominates the inertia of the entrained pairs. Section 4 outlines the effects of reheating in an optically thin, magnetized jet on the electron and photon distributions. We review the origin of a strongly anisotropic particle distribution in Section 5, and why the reabsorption of cyclo-synchrotron photons cannot effectively isotropize the pairs during delayed reheating.

Direct kinetic calculations of the photon and charged particle distributions are described in Section 6. The results of these calculations are presented in Section 7, using as an initial condition the quasi-thermal GRB spectrum calculated in Paper I. The calculation is repeated in an expanding medium in Section 8.

The residual effect of the regenerated $e^{\pm}$ shell on the output spectrum is evaluated in Section 9 using the Monte Carlo approach described separately in (Thompson & Gill 2014b) (hereafter Paper III). Scattering by an optically thick shell is shown to have only a modest flattening effect on the low-energy spectrum, in contradiction with recent claims in the literature. We also test spectral models that invoke continuous heating starting at a modest scattering depth, and continuing across the photosphere. This is shown to produce strong soft-hard evolution that strongly contradicts the observed behavior.

The implications of our results are summarized in Section 10. Appendix A gives further details of our kinetic code, and Appendix B analyzes the different types of drag experienced by electrostatically heated particles in a magnetized plasma.

In mathematical expressions we use the shorthand $X_n \times 10^n$ to describe a quantity X in cgs units.

2. CHALLENGES FOR A MODEL OF THE PROMPT GAMMA-RAY EMISSION

Before presenting our spectral model, we set the stage by reviewing several challenges to a theoretical understanding of the prompt emission of GRBs.

2.1. *Origin of the spectral peak in GRBs*

A common early approach to the GRB emission problem was to imagine that all parts of the non-thermal spectrum originate in the same part of the outflow (e.g. Pe'er & Waxman 2004; Stern & Poutanen 2004; Giannios & Spruit 2005). Since the *high-energy* part of the spectrum must originate at a high Lorentz factor, this then implies that the spectral peak in the comoving frame is very low. Some fine tuning is required to avoid pushing the spectral peak to either very high or low values. This is especially an issue in synchrotron-self-Compton emission models.

As has been noted by a number of authors, a fireball forming at the engine and then diluted by adiabatic expansion is inconsistent with the spectral peaks of most GRBs, producing a peak at too high an energy (e.g. Rees & Mészáros 2005). Continuing dissipation in a plasma of a very high compactness naturally generates a spectral peak at $\hbar\omega'_{\rm pk} \sim 0.1 m_e c^2$ in the comoving frame through the exponential dependence of the pair density on temperature (Thompson 1997; Ghisellini & Celotti 1999; Eichler & Levinson 2000).

Detailed calculations (Paper I) show that this result i) is sensitive to the baryon loading, requiring a high magnetization $\sigma \gtrsim 10^5$ at jet breakout; and ii) also depends on distributed heating that is consistent with the damping of bulk hydromagnetic distortions of the jet fluid, but is probably not consistent with very localized heating by reconnection events. When heating is too fast, there is a rapid build-up of cold pairs which drive copious production of soft photons and a hardening of the low-energy spectrum.

Agreement with the observed spectra of GRBs is obtained if the bulk Lorentz factor is $\Gamma_{\rm br} \sim 1/\theta \sim$ 3-10 during this initial heating episode, as would be appropriate for breakout over an angular width θ:

$$\hbar\omega_{\rm pk} \sim \frac{4}{3}\Gamma_{\rm br} \times 0.1\ m_e c^2 \sim 200 \left(\frac{\Gamma_{\rm br}}{3}\right) \quad \text{keV}. \qquad (1)$$

In this approach, the low-energy part of the spectrum arises at a moderate radius, and is reprocessed to higher energies by delayed dissipation operating at a higher Lorentz factor and a larger radius. The origin of this delayed dissipation is one focus of this paper.

Baryons can dominate the photospheric opacity at breakout even when the magnetic energy still exceeds the baryon rest mass energy. Therefore even modest amounts of baryon contamination can force a transition from GRB to X-ray flash (Paper I). The cyclo-synchrotron process was found to be the largest source of seed photons in a plasma with $B^2/8\pi \gtrsim 0.1P$; otherwise double-Compton emission tends to dominate. The dependence of spectral peak on the parameters of a baryon-dominated jet with a weak magnetization has been considered by Beloborodov (2013); and over an intermediate range of magnetizations, with particular attention to cyclo-synchrotron emission, by Vurm et al. (2013). As these authors note, a baryon-dominated phase could still source the GRB spectral peak if the Lorentz factor were somewhat higher than argued for here, e.g. $\Gamma \gtrsim 30$.

2.2. *Role of Finite Scattering Depth*

The role of a scattering photosphere has played a somewhat nebulous role in modelling the spectra of GRBs. All emission mechanisms involving rapidly accelerated, non-thermal particles naturally lead to large scattering depths in $e^{\pm}$ pairs, if pushed to a large compactness (Guilbert et al. 1983; Mészáros & Rees 2000). Two drawbacks here are that i) the multiplication of the pair density can cut off the high-energy spectrum; and ii) will rapidly feed back on the energy of a synchrotron or inverse-Compton peak (with $\omega_{\rm pk}$ scaling as $(n_{e^+}/n_p)^{-2}$ or $(n_{e^+}/n_p)^{-4}$, respectively).

The second issue is a particularly serious one, since very bright GRBs with low-energy spectral peaks are not observed. Although the strong sensitivity of peak energy on pair density can be partly mitigated by introducing seed thermal photons (Pe'er et al. 2006), some fine tuning is required to avoid the appearance of a cooling spectrum $F_\omega \propto \omega^{-1/2}$ above the spectral peak (Ghisellini & Celotti 1999). In effect, the injected non-thermal particle spectrum must extend downward to sub-relativistic energies. If shocks are responsible, they must be sub-relativistic and, in turn, cannot efficiently convert bulk kinetic energy to radiation (Beloborodov 2000).

The pair density is naturally buffered to a moderate value $\sim$ 10 in a thermal gas, and therefore may play a role in the creation of the spectral peak (Thompson 1997; Ghisellini & Celotti 1999). Our calculations show that the low-energy spectrum is consistent with that of a GRB if the outflow is strongly magnetized (Paper I).

Runaway pair creation can mediate the formation of a high-energy gamma ray tail to a seed thermal spectrum, in a way that has only been briefly discussed in the GRB literature (Thompson 2006). Starting at a *low* scattering depth, but still high compactness, distributed heating of the plasma creates relativistic particles. The mean particle energy declines following a surge in pair creation, as the injected energy is shared amongst a greater number of particles. The inverse-Compton image of the seed thermal peak then scans through a broad range of energies.

The calculations presented here focus on this mechanism. We find that the created optical depth to scattering never exceeds $\sim$ 1-4, allowing the high-energy tail to connect smoothly to the thermal peak. The closest analog to this mechanism is synchrotron-self Compton emission by continuously heated pairs (Stern & Poutanen 2004): in the absence of seed thermal radiation the peak energy covers a broad range as the pair density develops.

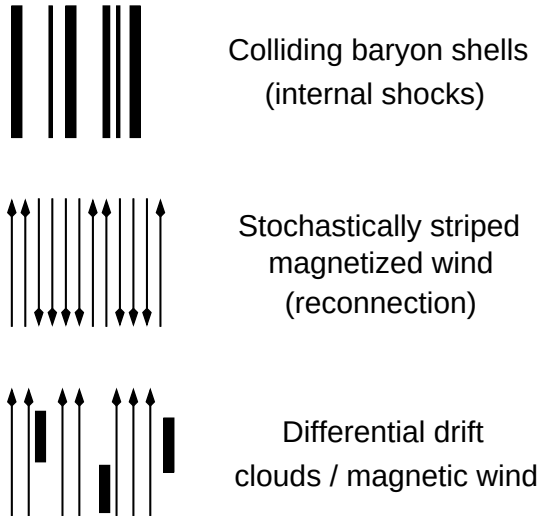

FIG. 1.— Variable gamma-ray emission from a relativistic outflow depends on some type of irregularity. A schematic of proposed mechanisms. 1. Differential motion of baryon shells. 2. Striping of a non-radial magnetic field. In a black-hole driven jet this field has a stochastic radial structure, imprinted by a dynamo process in the accreting material. 3. Differential motion of a magnetized jet with respect to baryon clouds that are swept up from an external medium. This third mechanism is distinguished from the others by depending on an intense radiation field: differential motion re-emerges below a radiation compactness $\sim 10^3$.

Continuous heating of the outflow (e.g. Drenkhahn & Spruit 2002) could, in principle, maintain a finite scattering depth in pairs over a very wide range of radius. The continuously created pairs are, however, very sensitive to any (temporary) shutoff in heating. The pairs mostly annihilate after such a shutoff, and the outflow is rapidly accelerated outward, leading to a freezeout of causal dissipative processes such as magnetic reconnection (Russo & Thompson 2013b). An additional argument against such an approach is provided by measurements of GRB pulse evolution: our Monte Carlo calculations (Section 9.1, Paper III) show that the pulses emerging from such a continuously heated photosphere are *broader* at higher energies, in strong contrast to the observed behavior.

2.3. *Powering the High-energy Emission*

Energy can be stored in a GRB fireball in the structure of the magnetic field (Thompson 1994; Spruit et al. 2001; Zhang & Yan 2011; McKinney & Uzdensky 2012) and in differential motion of baryon shells (Rees & Mészáros 1994; Kobayashi et al. 1997; Daigne & Mochkovitch 1998).

A third possibility (Figure 1) involves the differential motion of the magnetic field and baryons that are collected from the confining medium (Thompson 2006). Here we revisit the question of how these two components are accelerated, and in Paper III examine again how much mass is entrained by the magnetized jet. The

entrained baryons are light enough to be accelerated outward beyond breakout, but heavy enough to strongly disturb the magnetic field after both components have achieved relativistic expansion.

2.4. *Lorentz Factor Growth in the Outflow*

The photons and pairs in a simple, baryon-free fireball expand ballistically from the point of the 'explosion'. Here we consider what is, effectively, a radially offset explosion (actually multiple such explosions) with a significant contribution to the energy flux from an entrained magnetic field, and a subdominant contribution from baryon clumps at breakout.

The Lorentz factor profile of a magnetized jet while confined depends on the details of the confining medium. A common – but probably erroneous – assumption is that the jet moves into nearly free expansion once it leaves the vicinity of the engine. Such a rapid spreading would lead to rapid growth in Lorentz factor within a short distance outside the engine. But in a GRB, the neutron torus is itself the source of a trans-relativistic wind that is driven by neutrino annihilation heating on the torus surface (e.g. Dessart et al. 2009). Global simulations of accreting black holes that include the driving effect of magnetorotational heating (but not of such neutrino heating) show such an trans-relativistic sheath surrounding the relativistic jet core (Sądowski et al. 2013).

After breakout from a confining medium, a magnetized and pair-loaded jet rapidly becomes transparent and is accelerated outward by a combination of radiation pressure, and the Lorentz force due to diverging magnetic flux surfaces (Russo & Thompson 2013a,b).

2.5. *Radial Localization of the High-energy Emission Process*

Although the temporal power spectrum of a GRB is broad, representing pulses of a range of widths (Beloborodov et al. 2000), there is little evidence for systematic evolution of the power spectrum within a typical GRB – as might be expected if dissipation continued over decades in radius. The output of essentially all radiation processes depends on the plasma energy density and radiation compactness. The width of the emitted pulses is also sensitive to radius through the curvature delay of off-axis photons (Sari & Piran 1997), and through the changing size of dissipating zones, as limited by causal growth of inhomogeneities.

For these reasons, Thompson (2006) argued that the high-energy gamma-ray emission is triggered by a feedback process, and pointed to the interaction of the radiation field with ambient baryons. As the GRB outflow expands, the radiation field weakens and its compactness drops. The magnetic field is strongly perturbed by the differential motion of the baryons, with the timing of this interaction being determined by a reduction in the photon compactness below a critical value.

Two sources of the baryonic material can be considered: an external medium that formed before the collapse to a black hole; and denser material that is derived from the progenitor only after the collapse. The first is present to a significant degree only in collapsars, which emit powerful winds during a Wolf-Rayet phase. The second is present in both collapsars and binary neutron star mergers, because the merger product releases a dense neutron-rich wind before the collapse to a black hole, which extends to at least $\sim 10^9$ cm from the engine by the time the MHD jet is fully developed (Dessart et al. 2009).

Our focus, here and in Paper III, is on the second channel, baryons that are entrained by an MHD jet from a confining medium. When the co-moving radiation compactness is above $\ell_{\rm th} \sim (Y_e m_e/m_p)^{-1} \sim 4\times 10^3/Y_{e\,0.5}$, where $Y_e = 0.5 Y_{e\,0.5}$ is the electron fraction of the confining medium, baryons can be pushed outward by the intense radiation pressure. (Material derived from the surface of a Wolf-Rayet star typically has electron fraction $Y_e \sim 0.5$, whereas the neutron-rich outflow from the remnant of a binary neutron star merger is more electron poor, $Y_e \lesssim 0.1$: Dessart et al. 2009.) Acceleration of an MHD fluid containing a light $e^\pm$ gas can continue down to a much lower compactness, so that the baryons and magnetofluid develop a large differential Lorentz factor when the seed thermal radiation compactness has dropped to $\ell_{\rm th} \sim 10^2$-10^3.

2.6. *Nature of the Engine*

In this situation, a rapidly rotating magnetar is disfavored for a few reasons. First, the magnetized outflow is polluted by a neutron-rich wind from the hot neutron star surface (Duncan et al. 1986), and remains too dirty to support an ion magnetization as high as $\sim 10^5$ until an interval $\gtrsim 10^2$ s has lapsed (Metzger et al. 2011). Second, an orbiting torus that would help to collimate a polar jet is not excluded by centrifugal forces from the magnetar surface as it is from the horizon of a black hole. Indeed it requires fine tuning to supply enough angular momentum to the magnetar to power a long GRB without creating such a torus. Third, fine collimation of the jet (half-opening angle $\theta_j \lesssim 0.1$ rad) is required to puncture a CO core before it collapses (Lazzati et al. 2009, Paper III), which is difficult to achieve with a quasi-spherical outflow from a neutron star.

Even though the black hole in a GRB engine is surrounded by a very dense, neutron-rich torus, the baryon flux away from the horizon is easily suppressed by the back-pressure of a dense photon-electron-positron gas. Such a relativistic gas is injected into the jet funnel by annihilating neutrinos emitted by the torus, $\nu_e + \bar\nu_e \to e^+ + e^-$ (Eichler et al. 1989; Zalamea & Beloborodov 2011).

3. ACCELERATION OF AN OPTICALLY THIN AND STRONGLY MAGNETIZED SHELL

We consider a transient, magnetized outflow, of duration $t_{\rm eng}$, that is sourced by the horizon of a hyper-accreting black hole. The outflow contains a thermal radiation field, with a flat spectrum below the peak that is generated during an intermediate stage of heating during breakout (Paper I).

The baryonic magnetization is very high, $\sigma_{\rm ion} = B^2/4\pi\rho_{\rm ion}c^2 \gtrsim 10^5$ in the frame of the engine. The magnetic field B is predominantly non-radial over a wide range of radius. The rest mass density $\rho_{\rm ion}$ here refers only to baryons advected out from the black hole ergosphere. This constraint on $\sigma_{\rm ion}$ derives from the requirement that the relativistic component of the outflow is pair-dominated during breakout; otherwise the low-

energy spectrum is harder and the peak softer (Paper I, see also Vurm et al. 2013; Beloborodov 2013). In order to power the high-energy emission of a GRB, some component of the outflow other than thermal radiation carries much of the energy at breakout. Given that the density of embedded pairs is exponentially suppressed near breakout, the magnetic field can be viewed as a default choice.

The simplest case is a single pulse of activity of the central engine. One frequently encounters the idea that the engine may be sporadic, leading to radial structure in the outflow. In Paper III, we explore the role of angular variations in producing the pulse structure of GRBs, and the possibility that[1] T_{90} is much longer than $t_{\rm eng}$ as measured at jet breakout.

The outflow escapes a confining medium at a distance $R_{\rm br}$ from the engine, where 'br' labels breakout. We refer to this ambient medium in a generalized sense, because it can also be in bulk motion away from the engine (e.g. Ramirez-Ruiz et al. 2002). Deconfinement of a relativistic, magnetized fluid may even extend close to, or beyond, the transition between 'jet' ($\mathcal{R}_{\rm br} < 1$) and 'pancake' ($\mathcal{R}_{\rm br} > 1$) geometries:

$$R_{\rm br} \equiv \mathcal{R}_{\rm br} \cdot 2\Gamma_{\rm br}^2 ct_{\rm eng}. \tag{2}$$

Here $\Gamma_{\rm br}$ represents the Lorentz factor of the baryonic material through which the magnetized fluid is moving.

A corrugation instability is triggered in a forward baryon shell when it becomes geometrically thin, which is possible when the shell and the magnetofluid behind it expand to $\mathcal{R}_{\rm br} > 1$. Then, as is discussed further in Paper III, the duration of the gamma-ray emission is dominated by the curvature delay across the shell:

$$T_{90} \sim \mathcal{R}_{\rm br} t_{\rm eng}. \tag{3}$$

It should be noted that the numerical value of (2),

$$R_{\rm br} \sim 2\times 10^{11}\mathcal{R}_{\rm br}\left(\frac{\Gamma_{\rm br}}{3}\right)^2\left(\frac{t_{\rm eng}}{\rm s}\right)\ {\rm cm}, \tag{4}$$

can exceed the radius of the pre-existing 'envelope'. For a long GRB, this may be the radius of the Wolf-Rayet progenitor and, for a short GRB, the neutron-rich outflow that is emitted by a merged neutron star binary,

$$R_{\rm env} \sim \begin{cases} \lesssim R_\odot & ({\rm WR}), \\ ct_{\rm eng}/3 \sim 1\times 10^9\,(t_{\rm eng}/0.1\ {\rm s})\ {\rm cm} & ({\rm merger}). \end{cases} \tag{5}$$

The Poynting and radiation energy fluxes at breakout are expressed in terms of the compactness,

$$\ell_{\rm P,br} = \frac{\sigma_T}{m_e c^2}\frac{B'^2}{8\pi}\frac{R_{\rm br}}{\Gamma_{\rm br}}; \qquad \ell_{\rm th,br} = \frac{\sigma_T}{m_e c^2}U'_\gamma\frac{R_{\rm br}}{\Gamma_{\rm br}}, \tag{6}$$

as defined in the comoving (primed) frame. The apparent net energies carried by thermal radiation and magnetic Poynting flux are

$$E_{\rm P,iso} = \Gamma^2 B'^2 r^2 ct_{\rm eng}; \qquad E_{\gamma,\rm iso} = \frac{4}{3}\Gamma^2 U'_\gamma 4\pi r^2 ct_{\rm eng}. \tag{7}$$

[1] The standard measure of the duration of the prompt gamma-ray emission, encompassing 90% of the fluence.

Then

$$\ell_{\rm P,br} = \frac{\sigma_T E_{\rm P,iso}}{16\pi\mathcal{R}_{\rm br}\Gamma_{\rm br}^5 m_e c^4 t_{\rm eng}^2}; \qquad \ell_{\rm th,br} = \frac{3}{2}\frac{E_{\gamma,\rm iso}}{E_{\rm P\,iso}}\ell_{\rm P,br}. \tag{8}$$

Numerically, this works out to

$$\ell_{\rm th,br} = \frac{1\times 10^8}{(\mathcal{R}_{\rm br}/10)}\left(\frac{E_{\gamma,\rm iso}}{10^{52}\ {\rm erg}}\right)\left(\frac{\Gamma_{\rm br}}{3}\right)^{-5}\left(\frac{t_{\rm eng}}{\rm s}\right)^{-2}. \tag{9}$$

The radiation luminosity, normalized here at breakout, continues to grow as the magnetized component is accelerated outward by the Lorentz force (Section 3.2); and after the embedded pairs are reheated (Sections 4-7).

Although the breakout compactness increases in proportion to $E_{\rm iso}$, it also has a strong inverse dependence on $\Gamma_{\rm br}$. If the angle-integrated burst energy is regulated by the binding energy of the core (Thompson et al. 2007), which varies weakly with progenitor mass, and if breakout occurs in a causal manner on an angular scale $\delta\theta$, then $\Gamma_{\rm br}\,\delta\theta \sim 1$. For a single pulse, one has $E_{\rm iso}(\delta\theta)^2 \sim E_{\rm iso}/\Gamma_{\rm br}^2 \sim$ const, and so

$$\ell_{\rm br} \propto E_{\rm iso}^{-3/2}. \tag{10}$$

One sees that more luminous GRBs can be inferred to have a lower breakout compactness.

3.1. *Acceleration of Matter by Anisotropic Photon Pressure Outside Breakout*

Once the outflow becomes optically thin, the photon component self-collimates and defines a frame in which entrained particles move relativistically. In this section, we proceed first by neglecting the Lorentz force and the inertia of the magnetic field.

The net radiation force vanishes in a frame moving with Lorentz factor

$$\Gamma_{\rm eq}(r) \simeq \Gamma_{\rm br}\left(\frac{r}{R_{\rm br}}\right). \tag{11}$$

Then the radial flow of the entrained electrons and positrons closely approximates $\Gamma \simeq \Gamma_{\rm eq}$ until $\ell_{\rm th}$ drops below unity. Since

$$\ell_{\rm th}(r) = \ell_{\rm th,br}\left(\frac{r}{R_{\rm br}}\right)^{-1}\left(\frac{\Gamma}{\Gamma_{\rm br}}\right)^{-3}, \tag{12}$$

one finds that Γ saturates at

$$\begin{aligned}\Gamma_{\rm sat} &\sim \Gamma_{\rm br}\,(\ell_{\rm th,br})^{1/4} \\ &= 600\,\frac{(f_{\rm th,br}E_{j,51})^{1/4}}{(t_{\rm eng}/{\rm s})^{1/2}(\Gamma_{\rm br}\theta_j)^{1/2}}\left(\frac{\Gamma_{\rm br}/3}{\mathcal{R}_{\rm br}}\right)^{1/4}\end{aligned} \tag{13}$$

at a radius

$$\begin{aligned}R_{\rm sat} &= \frac{\Gamma_{\rm sat}}{\Gamma_{\rm br}}\,R_{\rm br} \\ &= 5.4\times 10^{14}\left(\frac{\mathcal{R}_{\rm br}t_{\rm eng}}{10\ {\rm s}}\right)\left(\frac{\ell_{\rm th,br}}{10^8}\right)^{1/4}\left(\frac{\Gamma_{\rm br}}{3}\right)^2\ {\rm cm}.\end{aligned} \tag{14}$$

Here, for illustration, we have re-written $E_{\gamma,\rm iso} = (2/\theta_j^2)f_{\rm th,br}E_j$, where E_j is the total (bi-axial) jet energy and a fraction $f_{\rm th,br}$ is carried by thermal photons at breakout.

3.2. *Acceleration of a Very Strongly Magnetized Outflow with Frozen MHD Turbulence*

Now we take into account the Lorentz force acting on a magnetized outflow, and its interaction with the radiation force. Both of these forces are calculated using the formalism of Russo & Thompson (2013b). The spreading of magnetic flux surfaces outside breakout is incorporated with a simple causal prescription, and the radiation force and $\Gamma_{\rm eq}$ are calculated by taking moments of the radiation field in the small-angle approximation.

A non-radial magnetic field carried outward by a relativistic jet contributes negligible inertia beyond the fast magnetosonic surface, which sits at Lorentz factor $\Gamma \simeq \sigma^{1/3}$. The magnetization σ, as defined by the inertia of the embedded pairs, is formally very high at breakout. Then one must examine carefully other possible sources of inertia.

To illustrate how turbulence provides inertia, we first consider the expansion of a plane-symmetric, magnetized slab into a vacuum. We provide an analytic solution to the similarity problem posed by Granot et al. (2011), here generalized to include both cold matter and a background of Alfvén waves in the pre-expansion state. Then we generalize the calculation of jet breakout with radiation pressure by Russo & Thompson (2013b) to include the effects of frozen MHD turbulence. For the time being, we ignore any baryons derived from a confining medium.

3.2.1. *Self-similar Expansion of a Magnetized, Turbulent Slab*

Consider a semi-infinite medium, initially filling $x < 0$ and containing a uniform magnetic field $\mathbf{B} = B_0\hat{z}$ and perfectly conducting matter with proper density $\rho_0 \ll B_0^2/8\pi c^2$. Superposed on this relativistic magnetofluid is a gas of Alfvén waves of energy density $U_t = \varepsilon_t B^2/8\pi$. The usual magnetization parameter is $\sigma = B^2/4\pi\rho c^2$. The effective magnetization, taking into account the inertia of the turbulence, is

$$\sigma_{\rm eff} = \frac{B^2/4\pi}{U_t/2 + \Gamma\rho c^2} = \frac{\sigma}{\varepsilon_t\sigma/4 + 1}. \tag{15}$$

There is an additional factor of $1/2$ multiplying U_t because the component of the magnetic field that is parallel to the direction of the mean flow imparts a vanishing Lorentz force.

The medium begins to expand into a vacuum at $x > 0$ at time $t = 0$. We follow the expansion with velocity $\mathbf{v} = v\hat{x}$ using the similarity coordinate $\chi = x/ct$,

$$B = B_0\hat{B}\left(\frac{x}{ct}\right); \quad v = c\hat{v}\left(\frac{x}{ct}\right). \tag{16}$$

The $x-$component of the relativistic Euler equation is

$$\Gamma\rho\left[\frac{\partial(\Gamma v)}{\partial t} + v\frac{\partial(\Gamma v)}{\partial x}\right] = \frac{1}{c}(\mathbf{J}\times\mathbf{B})_x + \frac{\boldsymbol{\nabla}\cdot\mathbf{E}}{4\pi}E_x, \tag{17}$$

where $\mathbf{E}$, $\mathbf{B}$ denote electric and magnetic fields and $\mathbf{J}$ is the current density. The Lorentz force has contributions from both the background laminar fluid and the turbulence,

$$\frac{1}{c}(\mathbf{J}\times\mathbf{B})_x = -\frac{B}{4\pi}\left[\frac{\partial B}{\partial x} + \frac{1}{c}\frac{\partial E_y}{\partial t}\right] + \frac{1}{c}\langle B_{y,T}J_{z,T} - B_{z,T}J_{y,T}\rangle. \tag{18}$$

Here $\langle ...\rangle$ denotes a temporal and spatial average over quantities bilinear in the waves. Only the turbulence contributes to the Coulomb force in this planar geometry. Since $B'_{z,T} = E'_{z,T} = 0$ for Alfvén waves moving along the z-magnetic field in the co-moving frame, the wave fields in the lab frame are

$$\begin{aligned} &B_{x,T} = B'_{x,T}; \quad B_{y,T} = \Gamma B'_{y,T}; \quad B_{z,T} = \Gamma\frac{v}{c}E'_{y,T} \\ &E_{x,T} = E'_{x,T}; \quad E_{y,T} = \Gamma E'_{y,T}; \quad E_{z,T} = -\Gamma\frac{v}{c}B'_{y,T}. \end{aligned} \tag{19}$$

The net contribution to the Lorentz force from large-scale t- and x-derivatives of these fields is

$$\begin{aligned} F_t &\equiv \frac{1}{c}\langle(\mathbf{J}_t\times\mathbf{B}_t)_x\rangle + \frac{1}{4\pi}\left\langle\frac{\partial E_{x,T}}{\partial x}E_{x,T}\right\rangle \\ &= -\frac{1}{4\pi}\Bigg\langle\frac{1}{2}\frac{\partial}{\partial x}\left(B_{y,T}^2 + B_{z,T}^2 - E_{x,T}^2\right) \\ &\qquad + B_{z,T}\frac{1}{c}\frac{\partial E_{y,T}}{\partial t} - B_{y,T}\frac{1}{c}\frac{\partial E_{z,T}}{\partial t}\Bigg\rangle. \end{aligned} \tag{20}$$

The mean magnetic field is imprinted in the fluid, and evolves according to

$$\frac{\partial B}{\partial t} + \frac{\partial(vB)}{\partial x} = 0; \quad B = B_0\frac{\Gamma\rho}{\rho_0}. \tag{21}$$

We also need an equation of state for the turbulent pressure in the comoving frame. The pressure of Alfvén waves in an isotropically expanding plasma evolves in the same way as photons, but here there is no expansion parallel to the background field. Then the adiabatic invariant is

$$(B'_t)^2 \propto B' = \frac{B}{\Gamma}. \tag{22}$$

Making use of this relation and equations (19) and (21), assuming equal contributions from the two polarization modes, and approximating $E'_{x,T} = B'_{y,T}$ (as appropriate for Alfvén waves in a very strongly magnetized plasma), the turbulent Lorentz force (20) simplifies to

$$F_t = -\frac{\varepsilon_t}{4}\Gamma^3\frac{BB_0}{4\pi c^2}\left(\frac{\partial v}{\partial t} + v\frac{\partial v}{\partial x}\right). \tag{23}$$

The Euler equation becomes

$$\begin{aligned} &\left[\Gamma^3\left(\rho_0c^2 + \frac{\varepsilon_t}{4}\frac{B_0^2}{4\pi}\right) + \frac{BB_0}{4\pi}\right]\frac{\partial v}{\partial t} \\ &+ \left[\Gamma^3\left(\rho_0c^2 + \frac{\varepsilon_t}{4}\frac{B_0^2}{4\pi}\right) - \frac{BB_0}{4\pi}\right]v\frac{\partial v}{\partial x} = -\frac{1}{\Gamma^2}\frac{B_0}{4\pi}\frac{\partial B}{\partial x}. \end{aligned} \tag{24}$$

We see that the turbulence produces a simple re-scaling of the material energy density, corresponding to a magnetization (15).

In the remainder of this section, we provide a simple analytic solution, which can be applied to both the laminar and turbulent fluids. Substituting the ansatz (16) into equations (17) and (21) in combination with (20) and (22), and replacing σ_0 with $\sigma_{\rm eff,0}$, gives

$$\left[\Gamma^3(\hat{v} - \chi) - \sigma_{\rm eff,0}\chi\hat{B}\right]\frac{d\hat{v}}{d\chi} = -\sigma_{\rm eff,0}(1 - \chi\hat{v})\frac{d\hat{B}}{d\chi};$$

$$(\chi - \hat{v})\frac{d\hat{B}}{d\chi} = \hat{B}\frac{d\hat{v}}{d\chi}. \quad (25)$$

Combining these two equations gives a constraint on the evolved magnetic field,

$$\sigma_{\rm eff,0}\hat{B} = \Gamma^3\frac{(\chi-\hat{v})^2}{1-\chi^2}. \quad (26)$$

The inner boundary of the rarefaction wave is determined by setting $\hat{B}=1$ and $\hat{v}=0$, giving

$$x = -\left(\frac{\sigma_{\rm eff,0}}{1+\sigma_{\rm eff,0}}\right)^{1/2} ct. \quad (27)$$

This coincides with the position of a magnetosonic wave moving inward through the magnetofluid and starting at $x=0$ at $t=0$.

The solution for the velocity field is obtained by differentiating equation (26) with respect to the similarity variable χ, and then substituting into the second of equations (25), giving

$$\frac{d\hat{v}}{d\chi} = \frac{2(1-\hat{v}^2)}{3(1-\chi^2)}. \quad (28)$$

This integrates to give

$$\frac{1+\hat{v}}{1-\hat{v}} = \left[(1+\sigma_{\rm eff,0})^{1/2} + \sigma_{\rm eff,0}^{1/2}\right]\left(\frac{1+\chi}{1-\chi}\right)^{2/3}. \quad (29)$$

The coefficient has been determined by setting $\hat{v}=0$ at the inner boundary (27) of the rarefaction wave. The outer boundary of the wave coincides with $\hat{B}=0$, corresponding to $\hat{v}=\chi$.

The maximum Lorentz factor is reached at this boundary, and is found to be

$$\Gamma_{\rm max} \simeq 2\sigma_{\rm eff,0} \quad (\sigma_{\rm eff,0} \gg 1). \quad (30)$$

This agrees with the laminar solution of Granot et al. (2011), but with the important distinction that $\sigma_{\rm eff,0}$ is rescaled downward from σ_0. When the turbulent intensity $\varepsilon_t \gg 1/\sigma_0$, as is almost certainly the case in the applications considered here, one has

$$\sigma_{\rm eff,0} \simeq \frac{1}{\varepsilon_t}; \qquad \Gamma_{\rm max} \simeq \frac{2}{\varepsilon_t} \ll \sigma_0. \quad (31)$$

In the parts of the fluid which reach a high Lorentz factor, one finds

$$\Gamma = \sigma_{\rm eff,0}^{1/3}\left[\frac{1+\chi}{2(1-\chi)}\right]^{1/3} \qquad \chi \le 1-(4\sigma_{\rm eff,0})^{-2}. \quad (32)$$

Focusing on the thin, relativistic layer near the outer boundary ($\chi \simeq 1$), one finds for the magnetic and velocity fields,

$$B = \frac{B_0}{2}\left(1-\frac{\Gamma}{2\sigma_{\rm eff,0}}\right)^2; \quad \rho = \frac{\rho_0}{2}\left(1-\frac{\Gamma}{2\sigma_{\rm eff,0}}\right). \quad (33)$$

3.2.2. *Expansion of an Optically Thin, Turbulent Jet*

The jet material, now optically thin, accelerates outward by a combination of radiation pressure and the Lorentz force. Then the radial causal distance $\sim r/\Gamma^2$ shrinks in the background inertial frame. The angular causal distance $\sim r/\Gamma$ also shrinks if the increase in Γ is faster than linear (Tchekhovskoy et al. 2010; Russo & Thompson 2013b). Therefore MHD modes with wavelength $\sim r/\Gamma$, and especially those with a significant radial component, will become frozen into the flow, and only gradually be smoothed out by expansion.

The frozen turbulence behaves like a relativistic fluid. The enthalpy per scattering charge that is carried by the electromagnetic field is

$$w_{\rm P} = \frac{\hat{B}_p\cdot(\mathbf{E}\times\mathbf{B})}{4\pi n_e}. \quad (34)$$

Here $\mathbf{B}$ and $\mathbf{E}$ are the magnetic and electric fields, and n_e is the density of scattering charges, all evaluated in the inertial frame. $\hat{B}_p$ denotes the unit vector parallel to the poloidal magnetic field.

We work in the approximations that i) the flow is radial, with small angular deviations leading to a large Lorentz force; and ii) the background magnetic field is purely toroidal.[2] Then

$$w_{\rm P} = \frac{B_\phi^2+B_\theta^2}{4\pi n_e} = \bar{w}_{\rm P} + w_t, \quad (35)$$

where

$$\bar{w}_{\rm P} = \frac{\bar{B}_\phi^2}{4\pi n_e} \quad (36)$$

is the contribution from the mean flow, and

$$w_t = \frac{(\delta B_\phi)^2+(\delta B_\theta)^2}{4\pi n_e} \quad (37)$$

from the frozen turbulence.

We focus here on steady expansion, with a uniform rate of transfer of toroidal magnetic flux along a poloidal flow line,

$$\frac{\bar{B}_\phi}{n_e r\sin\theta} = \text{const}. \quad (38)$$

To obtain the scaling of w_t with radius, one notes that the wave field can be written as

$$\delta\mathbf{B}' = \frac{1}{r\sin\theta}\frac{\partial\boldsymbol{\xi}}{\partial\phi}B'_\phi \quad (39)$$

where $\boldsymbol{\xi}$ is the Lagrangian displacement field of the magnetofluid and the prime denotes the comoving frame. The gradient scales as r^{-1} under expansion, and $\xi^2 \propto 1/B'_\phi$, hence for a nearly radial flow

$$w_t \sim \frac{(\Gamma\delta B')^2}{4\pi n_e} \propto \frac{\Gamma^2 B'_\phi}{r^2 n_e} \propto \frac{\Gamma}{r}. \quad (40)$$

Therefore w_t evolves according to

$$\frac{1}{w_t}\frac{dw_t}{dr} = \frac{1}{\Gamma}\frac{d\Gamma}{dr} - \frac{1}{r}. \quad (41)$$

The turbulent energy per particle decays as r^{-1} in the comoving frame, but may even grow slightly in the inertial frame.

[2] Here we can neglect the mean radial magnetic field threading the jet, since it has expanded far beyond the speed-of-light cylinder of the engine.

It is common to express the relative partitioning between rest energy and magnetic energy in terms of the magnetization,

$$\sigma = \frac{(\bar{B}_\phi)^2}{4\pi n_e \mu c^2} = \frac{\bar{w}_{\rm P}}{\mu c^2}. \tag{42}$$

This can be written in terms of the magnetic compactness,

$$\ell_{\rm P}^{\rm lab} = \frac{dL_{\rm P}/d\Omega}{dL_\gamma/d\Omega}\,\ell_{\rm th}^{\rm lab} \tag{43}$$

where

$$\ell_{\rm th}^{\rm lab} \sim \frac{4}{3}\Gamma^3 \ell_{\rm th} \equiv \frac{\sigma_T}{\mu c^3 r}\frac{dL_\gamma}{d\Omega} \tag{44}$$

is the photon compactness in the inertial frame. Then (e.g. equation (14) of Russo & Thompson 2013b),

$$\sigma = \frac{\ell_{\rm P}^{\rm lab}}{6\Gamma^2 \tau_{\rm T}}, \tag{45}$$

where the scattering depth is evaluated for a radial ray in the Thomson approximation,

$$\tau_{\rm T}(r) = \int_r^\infty \frac{\sigma_T n_e}{2\Gamma^2} dr. \tag{46}$$

A minimal magnetization in a pair-dominated outflow is obtained by taking an inertia $\mu = 2m_p/Y_{e\,0.5}$. Then at breakout ($\tau_{\rm T} \sim 3$) one has

$$\sigma = 4\times 10^6\,\mathcal{R}_{\rm br}^{-1}\left(\frac{E_{\rm P}}{10^{52}\ {\rm erg}}\right)\left(\frac{\Gamma}{3}\right)^{-2}\left(\frac{t_{\rm eng}}{\rm s}\right)^{-2}. \tag{47}$$

The response of the outflow to an imposed radial force (such as radiation pressure) depends on σ in a subtle way. In a purely laminar outflow, the effective particle inertia is (e.g. Goldreich & Julian 1970; Russo & Thompson 2013b)

$$\mu_{\rm eff} = m_e\left(1 - \frac{\sigma}{\Gamma^3}\right) \quad (\sigma, \Gamma \gg 1). \tag{48}$$

This would be negative at breakout in an outflow with magnetization (47) and Lorentz factor $\Gamma \sim 3 - 10$.

At such large values of σ, the energy carried by the frozen turbulence dominates the kinetic energy of the entrained charges. Then the effective magnetization is obtained by replacing $\Gamma\mu c^2 \to w_t$,

$$\sigma_t \sim \left(\frac{B_\phi}{\delta B}\right)^2 \Gamma. \tag{49}$$

We focus here on the case where the turbulent intensity at breakout is large enough to ensure $\sigma_t < \Gamma^3$. Then we can work with the total energy integral

$$w = \Gamma\mu c^2 + \bar{w}_{\rm P} + w_t + \mathcal{R}, \tag{50}$$

where

$$\mathcal{R} \simeq \frac{1}{n_e \mu c^3 r^2}\frac{dL_\gamma}{d\Omega} = \frac{\ell_{\rm th}^{\rm lab}}{\sigma_T n_e r} \tag{51}$$

is the energy per particle that is carried by radiation, in units of $m_e c^2$. The photons have energies around $0.1 m_e c^2$ in the comoving frame (Paper I), so we focus here on Thomson scattering with cross section σ_T. Then from equation (32) of Russo & Thompson (2013b),

$$\frac{d\mathcal{R}}{dr} = \frac{\sigma_T n_e}{4\Gamma^2}\left[\left(\frac{\Gamma}{\Gamma_{\rm eq}}\right)^4 - 1\right]\mathcal{R}. \tag{52}$$

We work in the regime where w_t, $\bar{w}_{\rm P}$, and $\mathcal{R}$ are all much larger than unity. Then the kinetic term in (50) can be neglected, and making use of the scaling (40), one finds that $dw/dr = 0$ gives

$$\frac{d\Gamma}{dr} = \frac{\Gamma}{r} - \frac{\Gamma}{w_t}\left(\frac{d\mathcal{R}}{dr} + \frac{d\sigma}{dr}\right). \tag{53}$$

The change in magnetization is driven mainly by angular spreading of the magnetic field lines (Tchekhovskoy et al. 2010, and references therein). Equation (38) may be used to reference σ to its value at breakout,

$$\sigma = \sigma_{\rm br}\frac{r\sin\theta}{(r\sin\theta)_{\rm br}}\frac{\bar{B}_\phi}{\bar{B}_{\phi,{\rm br}}}, \tag{54}$$

and taking the small-angle limit for the polar angle of a poloidal flux surface, $\theta = \delta\theta + \theta_{\rm br}$, one finds

$$\sigma = \sigma_{\rm br}\frac{1 + \delta\theta/\theta_{\rm br}}{1 + d(\delta\theta)/d\theta_{\rm br}} \tag{55}$$

The change in σ due to angular spreading can, in general, be of either sign. We focus here on parts of the outflow where σ decreases with radius, corresponding to

$$\frac{d\sigma}{dr} \sim -\sigma\frac{|\beta_\theta|}{\theta_{\rm br} r}. \tag{56}$$

The angular velocity is allowed to grow only at a causal rate,

$$\frac{d|\beta_\theta|}{dr} \sim \frac{1}{\Gamma r}. \tag{57}$$

Finally we must evaluate the change in the equilibrium frame of the radiation field. One has $\Gamma_{\rm eq} \propto r$ in a freely expanding radiation field. We follow the procedure of Russo & Thompson (2013b) and take angular moments of the radiation field,

$$F_n = \frac{1}{2}\int d\mu (1-\mu)^n \frac{1}{r^2}\frac{dL_\gamma}{d\Omega}(\mu). \tag{58}$$

Then $\Gamma_{\rm eq}^2 = F_0/4F_1$, and by combining equations (30) and (31) of Russo & Thompson (2013b), one finds

$$\left(\frac{\Gamma_{\rm eq}}{r}\right)^{-1}\frac{d}{dr}\left(\frac{\Gamma_{\rm eq}}{r}\right) = \left(\frac{\Gamma_{\rm eq}^2}{\Gamma^2} + \frac{1}{2}\right)\frac{1}{\mathcal{R}}\frac{d\mathcal{R}}{dr}. \tag{59}$$

A closed set of equations describing the acceleration of a hot, magnetized jet outside breakout is provided by (41), (52), (53), (56), (57), and (59). The value of n_e at breakout is iterated to give a pre-determined value $\tau_{\rm T}(R_{\rm br})$.

The profile of magnetization, turbulent energy, and radiative energy per particle is shown in Figure 2, for an outflow with optical depth $\tau_{\rm res} = 3$ at breakout, Lorentz factor $\Gamma = 10$, and jet opening angle $\theta = \Gamma^{-1}$. The

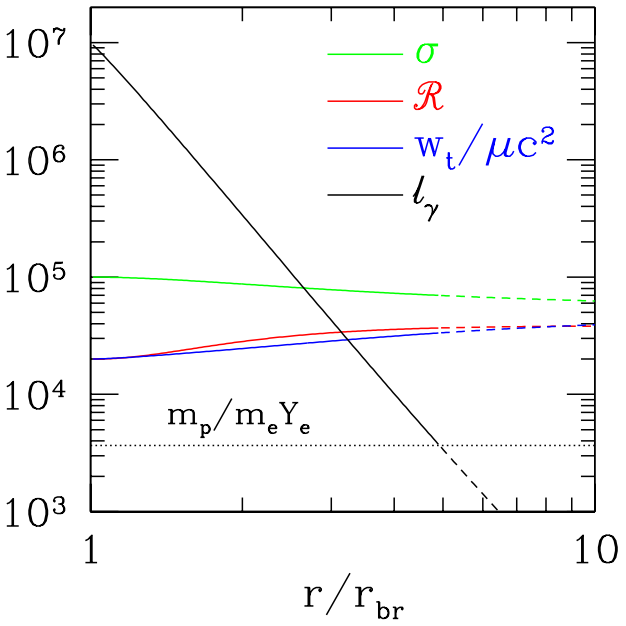

FIG. 2.— Various components of the energy of a magnetized jet as a function of distance outside breakout from a confining medium. At breakout, scattering depth $\tau(R_{\rm br} \to \infty) = 3$; magnetization (Poynting energy/particle rest energy) $\sigma = 10^5$; and both the radiation energy $\mathcal{R}$ and turbulent energy $w_t/\mu c^2$ equal to 0.2σ. Curves are dashed outside the radius (64) at which growth of the matter Lorentz factor stalls, but continuing acceleration of the magnetized jet is still possible.

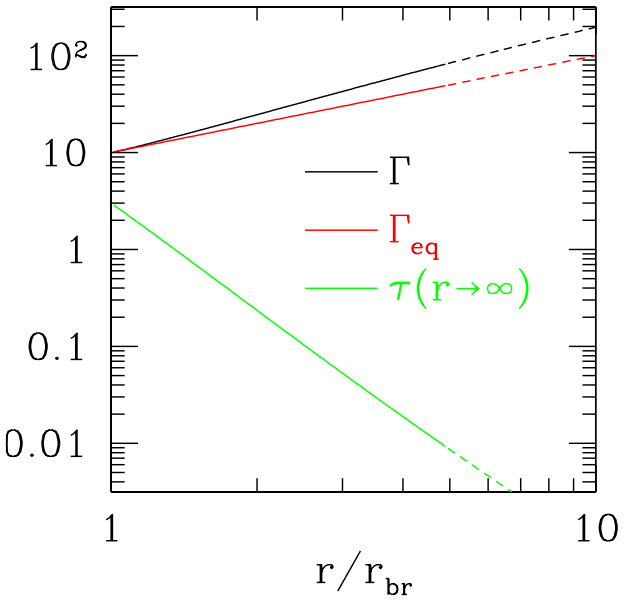

FIG. 3.— Lorentz factor Γ of the outflow shown in Figure 2. $\Gamma_{\rm eq}$ defines the frame in which the radiation force vanishes. Electron scattering optical depth is measured from radius r to infinity.

growth of Lorentz factor, shown in Figure 3, is somewhat faster than linear ($d\ln\Gamma/d\ln r \simeq 1.4$), and slightly outstrips the growth of $\Gamma_{\rm eq}$.

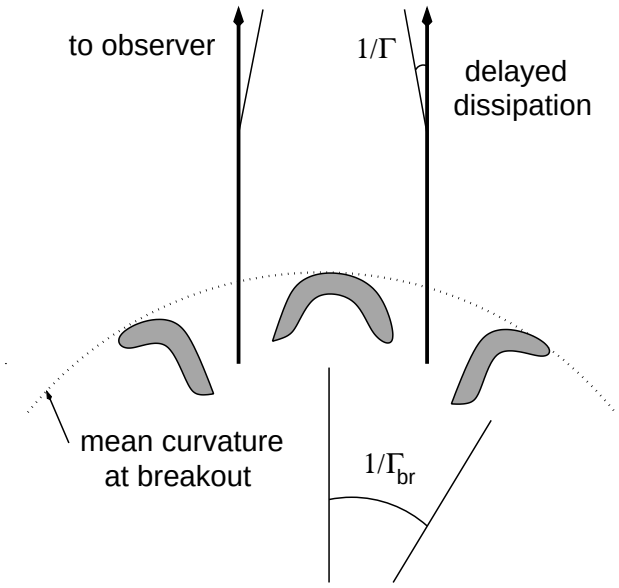

FIG. 4.— Shocked material derived from the confining medium experiences a corrugation instability at breakout, once the contact discontinuity accelerates to $\Gamma_c \sim 1/\theta_j$. Magnetized material escaping through holes in the corrugated shell deviates from purely radial flow by an angle $\delta\theta \sim 1/\Gamma_c$. Causal contact is then lost across an angle $\sim \theta_j$ as the magnetized material accelerates beyond breakout. When dissipation resumes at a larger radius (64), overlapping gamma ray pulses can result from causally separated events.

4. DISTRIBUTED HEATING IN A MEDIUM OF LOW INITIAL OPTICAL DEPTH

We now illustrate how a high-energy, non-thermal spectrum is generated by pair breakdown in a magnetized plasma containing a thermal photon seed. Detailed kinetic calculations are described in Sections 6, 7, and 8.

4.1. *Delayed Decoupling between Baryons and the Relativistic Components of the Outflow*

A hyperluminous, magnetized jet that breaks through a cloud of baryonic material can entrain a certain mass of baryons in spite of the corrugation instability that the baryons suffer at the jet head. The radiation field entrains baryons if they are thin enough to cool radiatively on the dynamical time, with a scattering depth

$$\tau_{\rm T,cool} \lesssim \left(\frac{3\ell_{\rm P,br}}{\Gamma_{\rm br}}\frac{m_e Y_e}{m_p}\right)^{1/2}. \qquad (60)$$

Here $\ell_{\rm P,br} = (\sigma_T/m_e c^2)(R_{\rm br}/\Gamma_{\rm br})B'^2/8\pi$ is the compactness of the magnetized outflow, measured in the comoving frame at breakout. Then the rest-mass luminosity at breakout can be related to the Poynting luminosity in a straightforward way (equation (24) of Paper III),

$$\left.\frac{\langle dL_{\rm rest}/d\Omega\rangle}{dL_P/d\Omega}\right|_{\rm br} = \frac{f_{\rm cover}\cdot R_{\rm br}^2\Sigma_b c^2}{t_{\rm eng}\,dL_P/d\Omega} = \frac{3 f_{\rm cover}\mathcal{R}_{\rm br}}{2\Gamma_{\rm br}^2\tau_{\rm T,cool}}. \qquad (61)$$

Here $f_{\rm cover}$ is the angular covering factor of the residual shells of baryons, and $\mathcal{R}_{\rm br}$ is the dimensionless breakout radius (2). Because the compactness at breakout (9) is still very large, this thin baryonic material remains optically thick, $f_{\rm cover}\tau_{\rm T,cool} \gg 1$.

As the jet Lorentz factor grows, there is a contraction in the angular distance over which a causal disturbance can propagate,

$$r\frac{d\theta}{dr} \sim \Gamma^{-1}. \tag{62}$$

This means that parts of the outflow containing clumps of entrained baryons, and those which do not, can become causally separated. Clumps of a typical size and separation $\delta\theta_{\rm br}$ at breakout will lose contact when the outflow has expanded to a Lorentz factor $\Gamma > 1/\delta\theta_{\rm br}$.

Once the (comoving) radiative compactness drops below

$$\ell_{\rm th} \sim \frac{m_p}{Y_e m_e}, \tag{63}$$

the parts of the jet containing baryons are no longer accelerated outward by the anisotropic photon pressure.

The limiting Lorentz factor depends on the radial flow profile. Here we choose a simple power-law expansion law, $\Gamma = \Gamma_{\rm br}(r/R_{\rm br})^{\delta}$. Then the compactness and scattering depth decrease as $\ell_{\rm th} = \ell_{\rm th,br}(r/R_{\rm br})^{-1-3\delta}$ and $\tau_{\rm T} = \tau_{\rm T,br}(r/R_{\rm br})^{-1-2\delta}$. The compactness reaches the limiting value (63) at the radius

$$R_{\rm sat,ei} \sim \left(\frac{m_e Y_e}{m_p}\ell_{\rm th,br}\right)^{-1/(1+3\delta)} R_{\rm br}, \tag{64}$$

where the Lorentz factor has grown to

$$\Gamma_{\rm sat,ei} = \left(\frac{Y_e m_e}{m_p}\right)^{1/4}\Gamma_{\rm sat} = 0.13\, Y_{e\,0.5}^{1/4}\Gamma_{\rm sat} \tag{65}$$

in the simplest case of linear expansion ($\delta = 1$).

The flow develops strong inhomogeneities in Lorentz factor beyond the radius (64), because the baryon-free parts of the jet continue to accelerate outward. Disturbances from the parts of the flow with Lorentz factor (65) propagate inward to the faster components at a rate

$$\delta\theta(r) \sim \frac{1}{\Gamma_{\rm sat,ei}}\ln\left(\frac{r}{R_{\rm sat,ei}}\right) \quad (r > R_{\rm sat,ei}). \tag{66}$$

In this way, the energy source for the high-energy part of the photon spectrum is *dynamically generated* outside the inner thermalization zone described in Paper I.

4.2. *Available Energy*

An important constraint on the reheating mechanism that generates the high-energy tail of a GRB is that the tail emission typically carries comparable energy to the part of the spectrum at or below the thermal peak. For example, our kinetic calculations show that the photon index is ~ -2.3 when the injected energy is about twice the seed thermal photon energy. The kinetic energy of the embedded baryons, as driven by the outward thermal photon flux inside the reheating zone, is limited by multiple scattering to

$$\frac{dL_k}{d\Omega} = \Gamma\frac{dL_{\rm rest}}{d\Omega} \lesssim \frac{dL_{\rm th}}{d\Omega}. \tag{67}$$

After decoupling of the matter from the photons, the magnetofluid continues to accelerate outward, so that its Lorentz factor exceeds the saturation Lorentz factor (13) of the baryons,

$$\Gamma_{\rm mag} \sim \frac{r}{R_{\rm sat,ei}}\Gamma_{\rm sat,ei}. \tag{68}$$

In the frame of the magnetofluid, the baryons move with a Lorentz factor

$$\Gamma'_{\rm ei} = \frac{1}{2}\left(\frac{\Gamma_{\rm sat,ei}}{\Gamma_{\rm mag}} + \frac{\Gamma_{\rm mag}}{\Gamma_{\rm sat,ei}}\right) \tag{69}$$

and their density is $\rho'_{\rm ion} = (\Gamma'_{\rm ei}/\Gamma_{\rm sat,ei})\rho_{\rm ion}$. Hence the energy available to heat the embedded pairs is

$$\begin{aligned}\frac{U'_{\rm heat}}{U'_{\rm th}} \sim \frac{\Gamma'_{\rm ei}\rho'_{\rm ion}c^2}{U'_{\rm th}} &\sim \frac{1}{4}\left(\frac{\Gamma^2_{\rm mag}}{\Gamma^2_{\rm sat,ei}} + 1\right)^2 \frac{dL_k/d\Omega}{dL_{\rm th}/d\Omega} \\ &\lesssim \frac{1}{4}\left[\left(\frac{r}{R_{\rm sat,ei}}\right)^2 + 1\right]^2.\end{aligned} \tag{70}$$

This bound is saturated only if outflow carries enough baryonic material. To check this, we start with the ratio (61) of rest luminosity to Poynting luminosity at breakout, substitute expression (60) for the scattering depth and (65) for the limiting baryon Lorentz factor, to get

$$\begin{aligned}\frac{dL_k/d\Omega}{dL_{\rm th}/d\Omega} &\le \Gamma_{\rm sat,ei}\frac{dL_{\rm rest}/d\Omega}{dL_{\rm th}/d\Omega} \\ &= 1.2\,\frac{f_{\rm cover}}{Y_{e\,0.5}^{1/4}}\,\frac{\mathcal{R}_{\rm br}/10}{(\Gamma_{\rm br}/3)^{1/2}}\,\frac{(\ell_{\rm P,br}/10^9)^{1/2}}{(\ell_{\rm th,br}/10^8)^{3/4}}.\end{aligned} \tag{71}$$

The result depends weakly on the compactness at breakout (as $\sim \ell^{-1/4}$) as well as on the thermalization efficiency $\ell_{\rm th}/\ell_P$. A combination of covering factor and shell expansion factor corresponding to $f_{\rm cover}\mathcal{R}_{\rm br} \gtrsim 10$ is required for efficient heating. Note that we have normalized the engine lifetime in the breakout compactness (9) to $t_{\rm eng} \sim 1$ s, when then implies an expansion factor $\mathcal{R}_{\rm br} \sim 10$ in a burst with $T_{90} \sim 10$ s.

We also note that increasing the isotropic energy tends to a *reduce* the outbreak compactness (equation (10)), which then raises the right-hand-side of equation (71). An evaluation of $f_{\rm cover}$ requires a numerical simulation along the lines of (Jiang et al. 2013), but including relativistic hydrodynamics and a magnetic field.

4.3. *Optical Depth of the Frozen Pairs*

The optical depth of the residual pairs in the magnetized jet has an important influence on the radiative signature of delayed heating. During jet breakout, annihilation freezes out and the scattering depth (46) evolves mainly by expansion below $\tau^{\pm}_{\rm T}(R_{\rm br}) \sim 3$,

$$\tau^{\pm}_{\rm T}(r) \simeq \tau^{\pm}_{\rm T}(R_{\rm br})\left(\frac{r}{R_{\rm br}}\right)^{-1}\left(\frac{\Gamma}{\Gamma_{\rm br}}\right)^{-2}. \tag{72}$$

At the radius (64) the depth through the frozen pairs has decreased to

$$\tau^{\pm}_{\rm T}(R_{\rm sat,ei}) \sim \tau_{\rm T,br}\left(\frac{m_e Y_e}{m_p}\ell_{\rm th,br}\right)^{-(1+2\delta)/(1+3\delta)}. \tag{73}$$

This works out to

$$\tau_{\rm T}^{\pm}(R_{\rm sat,ei}) \sim 1.4\times10^{-3}\,\left(\frac{\tau_{\rm T,br}}{3}\right)\left(\frac{\ell_{\rm th,br}}{10^8}\right)^{-3/4} \quad (74)$$

in the case of linear acceleration ($\delta = 1$).

4.4. *Pair Breakdown and Inverse Compton Spectrum*

We describe the heating by a volumetric input $dU_{\rm heat}/dt$ that extends over a total time $t_{\rm tot} \ll r/\Gamma c$,

$$\frac{dU_{\rm heat}}{dt} = \frac{\Delta U_{\rm heat}}{t_{\rm tot}}\left(\frac{t}{t_{\rm tot}}\right)^{-\alpha_h}. \quad (75)$$

In this section all quantities are evaluated in the comoving frame. The net heat released can be expressed in terms of a total compactness $\ell_{\rm heat}$, which accumulates from some initial time $t_0 < t_{\rm tot}$ according to

$$\frac{\ell_{\rm heat}(t)}{\ell_{\rm heat}} = \begin{cases} \ln(t/t_0)/\ln(t_{\rm tot}/t_0), & \alpha_h = 1 \\ (1-(t/t_0)^{1-\alpha_h})/(1-(t_{\rm tot}/t_0)^{1-\alpha_h}), & \alpha_h \neq 1 \end{cases} \quad (76)$$

In the initial state of the plasma considered here ($\tau_{\rm T} \sim 10^{-3}-10^{-2}$, the advected pairs quickly become relativistic after the onset of heating. They begin to upscatter the advected thermal photons to energies exceeding m_ec^2 in the comoving frame.

At a high radiative compactness (we consider an initial thermal compactness $\ell_{\rm th} \sim 300 - 10^3$), particle heating and cooling are in near balance and adiabatic losses can be neglected. Then

$$\frac{4}{3}(\gamma_e^2-1)n_e\sigma_T U_\gamma c = \frac{dU_{\rm heat}}{dt}, \quad (77)$$

where γ_e is the Lorentz factor of the pairs in the comoving frame. In the kinetic calculation described below, we find a nearly mono-energetic distribution while the particles are relativistic. During the first stages of heating, $U_\gamma \sim U_{\rm th}$, the seed thermal photon energy density. So

$$\frac{4}{3}(\gamma_e^2-1) = \frac{1}{\tau_{\rm T}}\frac{\Delta U_{\rm heat}}{U_{\rm th}}\left(\frac{t}{t_{\rm tot}}\right)^{-\alpha_h} = \frac{t_{\rm tot}}{\tau_{\rm T}\ell_{\rm th}}\frac{d\ell_{\rm heat}}{dt}, \quad (78)$$

where $\tau_{\rm T} \equiv n_e\sigma_T c t_{\rm tot}$ in this section.

The inverse-Compton image of the thermal peak during this first stage of heating sits at a comoving energy $\hbar\omega_{\rm IC,pk} \sim \frac{4}{3}(\gamma_e^2 - 1)\hbar\omega_{\rm pk}$. The initial seed peak is produced during a very compact thermalization phase before breakout (Paper I), with an energy $\hbar\omega_{\rm pk} \sim 0.1 m_ec^2$. Following this episode, the radiation is trapped by a forward baryon shell for an expansion factor as long as $\sim \mathcal{R}_{\rm br}$ while the Lorentz factor of the shell remains approximately constant. The corresponding adiabatic diluation of the peak energy in the comoving frame is in the range

$$1 \gtrsim f_{\rm ad} \gtrsim 0.2\left(\frac{\mathcal{R}_{\rm br}}{10}\right)^{-2/3}. \quad (79)$$

After breakout, we focus on the simplest case of linear growth of Γ, corresponding to $\omega_{\rm pk} \propto r^{-1}$.

Combining these effects, the comoving peak energy drops to

$$\hbar\omega_{\rm pk} \sim 0.1\ m_ec^2\,f_{\rm ad}\left(\frac{r}{R_{\rm br}}\right)^{-1}$$

$$\sim 0.008\ m_ec^2\,f_{\rm ad}\left(\frac{\ell_{\rm th,br}}{10^8}\right)^{-1/4}\left(\frac{r}{R_{\rm sat,ei}}\right)^{-1} \quad (80)$$

beyond the radius (64) where baryons and magnetic field begin to moving differentially. Heating at a particular place in the magnetofluid will typically be delayed beyond this transition, depending on the proximity of baryonic material. Substituting equations (72) and (73) into (78) gives the scaling $\hbar\omega_{\rm IC,pk} \propto (r/R_{\rm sat,ei})^2$, and

$$\frac{\hbar\omega_{\rm IC,pk}}{m_ec^2} \sim 3\,f_{\rm ad}\,\frac{\Delta U_{\rm heat}/U_{\rm th}}{(t/t_{\rm tot})^{\alpha_h}}\left(\frac{\ell_{\rm th,br}}{10^8}\right)^{1/2}\left(\frac{r}{R_{\rm sat,ei}}\right)^{2}. \quad (81)$$

This works out to $\hbar\omega_{\rm IC,pk} \sim 10\,f_{\rm ad}\,m_ec^2$, since we are considering moderately relativistic differential motion between the baryon-loaded and baryon-free parts of the outflow ($\Delta U_{\rm heat} \gtrsim U_{\rm th}$ and $r \sim 2R_{\rm sat,ei}$).

As photons accumulate above the pair-creation threshold, $\tau_{\rm T}$ begins to rise, reducing the equilibrium particle energy and eventually shutting off the source of pair-creating photons. Pair creation continues due to the accumulation of hard photons, and $\omega_{\rm IC,pk}$ drops toward the seed peak. A compactness $\ell_{\rm tot} = \ell_{\rm th} + \ell_{\rm heat} \sim 10^3$ is large enough to ensure that $\tau_{\rm T} > 1$ at the end of heating. Then the plasma enters a sub-relativistic state and, as we demonstrate in Section (7), the Compton upscattered peak merges smoothly with the seed thermal peak.

A first estimate of the high-energy spectral index is then obtained by relating the drop in $\omega_{\rm IC,pk}$ to the rise in optical depth. The energy spectrum can be written

$$\hbar\omega_{\rm IC}^2\frac{dn_\gamma}{d\omega_{\rm IC}} \sim \hbar\omega_{\rm IC}^2\frac{n_{\gamma,\rm pk}\,\sigma_T n_e c}{d\omega_{\rm IC}/dt}, \quad (82)$$

where

$$\frac{1}{\omega_{\rm IC}}\frac{d\omega_{\rm IC}}{dt} = \frac{1}{\gamma_e^2}\frac{d\gamma_e^2}{dt} = -\left(\frac{\alpha_h}{t} + \frac{1}{n_e}\frac{dn_e}{dt}\right). \quad (83)$$

Substituting equation (78) gives

$$\hbar\omega_{\rm IC}^2\frac{dn_\gamma}{d\omega_{\rm IC}} \sim \frac{\Delta U_{\rm heat}}{\alpha_h + d\ln n_e/d\ln t}\left(\frac{t}{t_{\rm tot}}\right)^{1-\alpha_h}. \quad (84)$$

For example, if $dn_e/dt \sim$ const, then $\omega_{\rm IC,pk} \propto t^{-1}$ and $\hbar\omega_{\rm IC}^2 dn_\gamma/d\omega_{\rm IC} \propto \omega_{\rm IC}^{-\alpha_h+1}$.

So far we have neglected the effects of expansion. These are included in Section 8 after we first examine the non-expanding case in some detail. It should be noted that, in the kinetic calculations described here, most of the non-thermal tail emerges on a modest fraction of $t_{\rm tot}$, which itself may be a fraction of the flow time $r/\Gamma c$.

5. RELATIVE IMPORTANCE OF INVERSE COMPTON AND SYNCHROTRON COOLING

Our focus here is on the simplest mechanism of distributed heating, by decaying turbulence. We are invoking essentially the same heating mechanism during the two main stages of spectral evolution. The qualitative difference in output spectrum (thermal vs. non-thermal) is mainly a consequence of the large drop in scattering depth after jet outbreak, as we explained in Section 4.

During the first stage of heating, leading to the formation of the spectral peak and the low-energy slope, there

is an indirect argument (Paper I) in favor of this mechanism over more sporadic and localized bursts of heating, such as might be mediated by magnetic reconnection. When the optical depth is high, the pairs remain subrelativistic if the heating is smooth, and the low-energy spectrum that emerges is much flatter than Planckian and comparable to that observed in a GRB. Localized and intense heating generates a higher pair density, which in turn pushes the Compton parameter much higher than in a thermal plasma, and allows the low-energy spectrum to push closer to Rayleigh-Jeans.

Decaying Alfvénic turbulence only heats the embedded $e^\pm$ along the magnetic field. At a high wavenumber, sheared Alfvén waves have the dispersion relation [3]

$$\omega^2(k_\parallel) = \frac{c^2}{\sqrt{1 + c^2 k_\perp^2/\omega_{Pe}^2}}. \tag{85}$$

Here $k_\perp, k_\parallel$ are the components of the wavevector perpendicular and parallel to the magnetic field, and ω_{Pe} is the electron plasma frequency. The waves therefore Landau damp on the longitudinal motion of the $e^\pm$ where $k_\perp \sim \omega_{Pe}c$, even while the wave frequency remains orders of magnitude below the electron cyclotron frequency $\omega_{ce} = eB/m_e c$.

The waves also become charge-starved during the first stages of reheating, in the sense that the fluctuating current density $\delta J \sim (c/4\pi)k_\perp \delta B$ exceeds the maximum conduction current $n_e e c$ at lower wavenumbers than those associated with Landau damping: see Thompson (2006) and Section 10.1.

Energy can also be transferred to small scales through an independent cascade that is mediated by the fast mode. In a strongly magnetized plasma, the fast mode closely approximates a vacuum electromagnetic wave, with isotropic dispersion relation $\omega \simeq ck$. The mode then carries a weak electric current compared with a sheared Alfvén mode of similar amplitude and wavenumber $k_\perp \sim k$. The fast waves damp rapidly at a frequency $\omega \sim kc \sim \omega_{Pe}$, via conversion to Langmuir waves, e.g. $f + f \to \ell + \ell$. In a relativistic plasma with magnetization $\sigma \gg 1$, the limiting fast wave frequency is then $\omega \simeq kc \sim \sigma^{-1/2}\omega_{ce} \ll \omega_{\rm ce}$. Once again, parallel heating of the embedded pairs is the main effect.

There is a close correspondence between fast turbulence and acoustic turbulence, for which the spectral energy density scales as $kU_k \sim k^{-1/2}$. Coincidentally this is the same scaling as has been obtained in most recent simulations of Alfvénic turbulence (Maron & Goldreich 2001; Boldyrev 2006). Hence fast waves and Alfvén could have comparable amplitudes at fixed $|k|$.

5.1. *Particle Heating in a Pair Plasma with Very Low $\beta = 8\pi P/B^2$*

The jet magnetization can be defined in two different ways, depending on whether the photon pressure is included in the material pressure. As regards the bulk dynamics of the jet, the photons are tied to the magnetic field inside breakout and contribute effectively to the plasma inertia; but outside breakout the two components have to be considered separately (Section 3).

The magnetization also influences plasma instabilities, such as firehose and cyclotron modes, that modify the particle distribution and operate on very short timescales. Here the photons can be ignored. The comoving plasma parameter is very small,

$$\beta \equiv \frac{8\pi n_e k_{\rm B} T_e}{B^2} \sim \frac{\tau_{\rm T}}{\ell_{\rm P}} \left(\frac{T_e}{m_e c^2}\right). \tag{86}$$

Using the scalings (12) for the compactness and (72) for the scattering depth, one has

$$\beta(r) \sim 1 \times 10^{-10} \frac{\Gamma(r)}{\Gamma_{\rm br}} \left(\frac{\tau_{\rm T,br}}{3}\right) \left(\frac{\ell_{\rm P,br}}{10^9}\right)^{-1} \left(\frac{3T_e}{0.1 m_e c^2}\right) \tag{87}$$

before the onset of reheating.

The pair pressure is somewhat higher during reheating,

$$\beta \sim \frac{8\pi n_e \gamma_e m_e c^2}{B^2} \sim \frac{1}{\gamma_e \ell_{\rm P}} \left(\frac{\Delta U_{\rm heat}}{U_{\rm th}}\right)^{1/2}. \tag{88}$$

Here $\ell_{\rm th} \lesssim m_p/(Y_e m_e) \sim 4 \times 10^3 Y_{e\,0.5}$, with $\ell_{\rm P} > \ell_{\rm th}$ to power the high-energy tail of a GRB, so $\beta \sim 10^{-3}/\gamma_e$.

We conclude that β is small enough during reheating that particle isotropization by cyclotron and firehose instabilities appears to be ineffective.

5.2. *Pitch Angle Excitation*

Even when the magnetic energy density dominates that stored in thermal radiation, $e^\pm$ which experience strong parallel heating will cool mainly by Compton scattering the radiation field. Once again we work in the frame in which the bulk plasma is at rest.

Synchrotron emission depends on excitation of the gyromotion. Coulomb scattering between relativistic electrons and positrons is negligible at low $\tau_{\rm T}$. Supposing that relativistic motion along the magnetic field is sustained by an electrostatic force, we can ask whether the equilibrium perpendicular temperature of the $e^\pm$ differs from the ambient color temperature T_c of low-energy photons.

In the presence of an isotropic, Rayleigh-Jeans spectrum of soft photons, a particle moving with speed $\beta_{e\parallel} c$ along $\mathbf{B}$ sees blackbody radiation of a temperature $T_c' \sim 2\gamma_{e\parallel} T_c$ in a cone of solid angle $\Delta\Omega' \sim \pi/\gamma_{e\parallel}^2$ in the rest frame of its guiding center. Here $\gamma_{e\parallel} = (1-\beta_{e\parallel}^2)^{-1/2}$. Since the particle re-radiates isotropically, it's equilibrium temperature is

$$T_\perp \sim \frac{T_c}{2\gamma_{e\parallel}}. \tag{89}$$

More effective gyro-heating is provided by multiple Compton scatterings of thermal photons, which operates in a diffusive manner. The gyrational momentum accumulated over a comoving time δt is (Thompson 2006)

$$p_\perp^2 \sim \frac{4}{5}\gamma_e^2 \left\langle \left(\frac{\hbar\omega}{c}\right)^2 \right\rangle \cdot n_\gamma \sigma_T c \delta t, \tag{90}$$

[3] This dispersion relation is modified when the particles have a relativistic dispersion along the magnetic field. Electron-supported modes such as whistlers and kinetic Alfvén waves are not present in the pair plasma because of its charge symmetry. Even if ions supply most of the positive charge, the dispersion relation remains equivalent to (85) at $k_\perp \sim \omega_{Pe}/c \gg k_\parallel$, as long as the magnetic energy dominates the rest energy of the electrons, $B^2/8\pi \gg n_e m_e c^2$.

and the corresponding pitch angle is

$$\frac{p_\perp}{\gamma_e m_e c} \sim \ell_\gamma^{1/2} \left(\frac{E_{\rm pk}}{m_e c^2}\right)^{1/2} \left(\frac{c\delta t}{r/\Gamma}\right)^{1/2}, \qquad (91)$$

where $E_{\rm pk} \simeq 3T_\gamma$ is the spectral peak energy and ℓ_γ the radiation compactness.

The gyrational state of the particles can, in some circumstances, maintain an equilibrium between synchrotron damping and excitation by Compton scattering. Self-absorption effects are important when the gyrational motion is mildly relativistic, $p_\perp \gtrsim m_e c$, and so we allow for a suppression of synchrotron emission by a factor $f_{\rm sa} < 1$. Synchrotron cooling damps only the perpendicular momentum of a particle, while leaving its gyrational rest frame unaltered. In this regime, $\gamma_e = \gamma_{e\,\parallel}(p_\perp/m_e c)$ and the synchrotron power is

$$\gamma_{e\,\parallel} c \frac{dp_\perp}{dt} = -2 f_{\rm sa} \left(\frac{p_\perp}{m_e c}\right)^2 \sigma_T \frac{B^2}{8\pi} c \qquad (p_\perp \gg m_e c). \qquad (92)$$

A self-consistent equilibrium

$$\frac{p_\perp}{m_e c} = \gamma_e^{3/4} \left(\frac{1}{3 f_{\rm sa}} \frac{E_{\rm pk}}{m_e c^2} \frac{U_\gamma}{B^2/8\pi}\right)^{1/4} \qquad (93)$$

is obtained as long as $p_\perp/m_e c \ll \gamma_e$. The synchrotron power (92) can be compared with the Compton power $(dE/dt)_{\rm IC} = (4\gamma_e^2/3)\sigma_T U_\gamma c$,

$$\frac{(dE/dt)_{\rm synch}}{(dE/dt)_{\rm IC}} = \frac{2 f_{\rm sa}^{1/2}}{(3\gamma_e)^{1/2}} \left(\frac{E_{\rm pk}}{m_e c^2}\right)^{1/2} \left(\frac{U_\gamma}{B^2/8\pi}\right)^{-1/2}. \qquad (94)$$

In the reheating zone, the comoving plasma parameters are $U_\gamma \lesssim B^2/8\pi$ and $E_{\rm pk} \sim 10^{-3} m_e c^2$, and so synchrotron losses are subdominant but not entirely negligible.

Low-frequency photons that are absorbed by exciting the gyrational motion of relativistic pairs contribute negligbly to the parallel drag force (Appendix B).

6. NUMERICAL METHOD

We now describe our approach to calculating the evolution of $e^\pm$ immersed in a thermal photon gas and subjected to continuous heating. Here and in Appendix A we use a simplified notation, with $n_\pm(p)$ representing the number density of $e^\pm$ pairs per dimensionless momentum p (in units of $m_e c$), and $n_\gamma(x)$ the number density of photons per dimensionless energy $x = \hbar\omega/m_e c^2$.

The state of the photo-pair plasma is governed by the following two integro-differential equations (e.g. Pe'er & Waxman 2005; Belmont et al. 2008; Vurm & Poutanen 2009)

$$\partial_t n_\pm(p) = \dot n_{\pm,{\rm cs}}(p) + \dot n_{\pm,{\rm pp}}(p) + \dot n_{\pm,{\rm pa}}(p) + \dot n_{\pm,{\rm coul}}(p) + \dot n_{\pm,{\rm heat}}(p) + \dot n_{\pm,{\rm exp}}(p) \qquad (95)$$

$$\partial_t n_\gamma(x) = \dot n_{\gamma,{\rm cs}}(x) + \dot n_{\gamma,{\rm pp}}(x) + \dot n_{\gamma,{\rm pa}}(x) + \dot n_{\gamma,{\rm exp}}(x) \qquad (96)$$

Here allowance is made for expansion, in the final term on the right-hand side, but there is no escape of photons and pairs. We describe the solutions in static and expanding boxes in Sections 7 and 8, respectively. The two distributions interact with each other and themselves via the processes of Compton scattering (cs, $\gamma + e^\pm \to \gamma + e^\pm$), pair production (pp, $\gamma + \gamma \to e^+ + e^-$), pair annihilation (pa, $e^+ + e^- \to \gamma + \gamma$), and Coulomb scattering (coul, $e^\pm + e^\pm \to e^\pm + e^\pm$).

The initial state is assumed to contain cold thermal pairs with a compactness $\ell_{e,0}$ along with soft thermal photons with a compactness $\ell_{\rm th}$. Heating of the pair gas is represented by the term $\dot n_{\pm,{\rm heat}}$ in equation (95), with a cumulative compactness $\ell_{\rm heat}$ injected by the end of the simulation.

The formation of a flat low-frequency spectrum by thermal Comptonization of cyclotron photons inside jet breakout has already been examined in Paper I. In the present calculations we take this 'thermal GRB' spectrum

$$\frac{dn_\gamma}{d\ln x} \propto \begin{cases} K x_{\rm pk}^3 \exp(-x_{\rm pk}/\theta_\gamma), & x < x_{\rm pk} \\ K x^3 \exp(-x/\theta_\gamma), & x \ge x_{\rm pk} \end{cases} \qquad (97)$$

as the input. The temperature $\theta_\gamma = k_{\rm B} T_\gamma/m_e c^2$ is a fit parameter, and during the initial heating phase differs slightly from the pair temperature. Equation (97) smoothly matches a flat low-energy spectrum, $dn_\gamma/d\ln x \propto x^0$ onto a Wien spectrum at energies above $x_{\rm pk} = 3\theta_\gamma$.

The system of interest has an elongated $e^\pm$ momentum distribution in the direction of the magnetic field (Section 5, Thompson 2006), but also a low to moderate scattering depth and significant inhomogeneity. The inhomogeneity is required to induce heating: our particular model involves large-amplitude distortions of the magnetic field by embedded baryon clouds (Paper III). The combination of inhomogeneity with a long mean free path for photons leads to some isotropization of the interactions.

The elongation of the $e^\pm$ distribution implies a suppression of cyclo-synchrotron emission (Section 5), which is difficult to handle quantitatively. Here we simply shut off synchrotron processes, and focus on Compton scattering of the seed thermal photons. Because the photon occupation number is everywhere small in the energy range calculated, we also neglect stimulated effects in Compton scattering.

By neglecting the anisotropy of the $e^\pm$, we also somewhat underestimate the rate of pair creation: photons that are Compton scattered by relativistic particles moving parallel to **B** are themselves beamed along the magnetic field, so that counterstreaming gamma rays have an enhanced center-of-momentum energy.

6.1. *Details of Time Evolution*

The evolution of the photon-pair plasma is divided into regimes of small and large energy exchange, as defined (e.g.) by the fractional energy shift of a photon after scattering. The Fokker-Planck (F-P) equations are used in the regime of small energy exchange, which for isotropic and homogeneous distributions can be written as (e.g. Nayakshin & Melia 1998)

$$\partial_t n_\pm^{\rm F\text{-}P}(p) = \partial_p \left[\frac{\gamma_e}{p} A_\pm n_\pm\right] + \frac{1}{2}\partial_p \left[\frac{\gamma_e}{p}\partial_p \left\{\frac{\gamma_e}{p} D_\pm n_\pm\right\}\right], \qquad (98)$$

$$\partial_t n_\gamma^{\rm F\text{-}P}(x) = \partial_x (A_\gamma n_\gamma) + \frac{1}{2}\partial_x^2 (D_\gamma n_\gamma). \qquad (99)$$

The coefficients $A_\pm(p,t)$, $A_\gamma(x,t)$ represent the average rate of change of particle or photon energy (due e.g. to secular cooling processes or expansion), and $D_\pm(p,t)$, $D_\gamma(x,t)$ are the corresponding diffusivities. Each of these terms receives contributions from Compton and Coulomb scattering, and the advection terms from expansion:

$$\{A,D\}_\pm = \{A,D\}_{\pm,\rm cs} + \{A,D\}_{\pm,\rm coul} + A_{\pm,\rm heat} + A_{\pm,\rm exp} \quad (100)$$

$$\{A,D\}_\gamma = \{A,D\}_{\gamma,\rm cs} + A_{\gamma,\rm exp}. \quad (101)$$

The F-P approach to Compton scattering is essentially equivalent to the standard Kompane'ets formalism (but with the stimulated term here neglected) and is essential for treating Coulomb collisions between thermal pairs.

The remaining interactions, including Compton scattering of soft photons by energetic particles (where photons receive a large energy boost, $\omega \to 4\gamma_e^2\omega_0$) are described by exact collision integrals over the two distributions. These integrals, and the division in energy and momentum space between the two time-evolution methods, is described in Appendix A. The full distribution functions are evolved by integro-differential equations combining both approaches:

$$\partial_t\{n_\pm,n_\gamma\} = \partial_t\{n_\pm,n_\gamma\}^{\rm F\text{-}P} + \partial_t\{n_\pm,n_\gamma\}^{\rm col}. \quad (102)$$

We choose to solve the coupled equations (98), (99) using the Chang & Cooper (1970) fully-implicit finite difference scheme, due to its robustness and guarantee of yielding positive spectra. This scheme is only accurate to first-order both in space and time, but much more stable than any of the higher order schemes (e.g. Park & Petrosian 1996). We use logarithmic grids for the particle distribution spanning five orders of magnitude ($p = 10^{-3} - 10^2$) in momentum and the photon distribution spanning eight orders ($x = 10^{-6} - 10^2$) in energy, with a grid size of 256 points for both distributions.

The Chang-Cooper scheme conserves particle number exactly by imposing the condition of vanishing flux at the grid boundaries. On the other hand, greater care must be taken in the numerical accuracy of the collision integrals, so as to avoid significant non-conservation of particle number. This is especially true for Compton scattering, where a double integral is carried out. To this end, we use adaptive quadrature routines to calculate the integrals exactly, rather than using methods such as the composite Simpson's rule, which is sufficient for all other interactions included in the simulation. This allows us to conserve particle number and energy to better than 1% in all the simulations presented in this study.

One advantage of using implicit schemes is that they are free from the Courant condition, which depends on the size of the smallest bin for logarithmic grids, on how large the time step can be. However, to ensure convergence to the right solution, the time step should be of the order of the fastest cooling time to accurately track diffusion of particles in energy space. Among all of the radiative processes considered here, particles cool predominantly by Compton scattering and the timescale of which scales with compactness of the photon field and particle energy:

$$t_{\rm cs} \sim \frac{t}{\gamma_e \ell_\gamma}. \quad (103)$$

This can be problematic for simulating highly compact plasmas, but for the values of ℓ_γ ($\sim 10^2 - 10^4$) used in this study, each run takes between a few minutes and few days on multiple processors.

7. DISTRIBUTED HEATING IN A STATIC MEDIUM

We can use the static approximation when the heating episode is brief compared with the flow time. The effect of scattering after the heating turns off can be evaluated with the Monte Carlo approach of Paper III, assuming a cold, frozen pair flow beyond the heating layer.

Our simulations start with the thermal GRB photon spectrum (97) and an initial photon compactness $\ell_{\rm th}$ that is determined by fixing i) the total compactness

$$\ell_{\rm tot} = \ell_{e,0} + \ell_{\rm th} + \ell_{\rm heat} \quad (104)$$

that has accumulated at the end of heating; and ii) the initial scattering depth $\tau_{T,0} = \sigma_T n_{e,0} c t_{\rm tot}$.

We consider both uniform heating, $\alpha_h = 0$ in equation (75), as well as heating distributed logarithmically over time ($\alpha_h = 1$). Heating therefore starts at a finite time $t_0 = 0.1 t_{\rm tot}$ and stops at time $t_{\rm tot}$.

The initial temperature of the pairs is set equal to θ_γ in equation (97), corresponding to a mean initial energy $\langle\gamma_{e,0}\rangle \simeq 1 + (3/2)\theta_\gamma$. The particle compactness is

$$\ell_{e,0} = \sigma_T c t_{\rm tot} U_{e,0} = \langle\gamma_{e,0}\rangle \tau_{\rm T,0}. \quad (105)$$

It is convenient to write the initial photon field compactness in terms of the total heating compactness,

$$\ell_{\rm th} = f_{\rm th}\ell_{\rm heat}, \quad (106)$$

so that

$$\sigma_T c t_{\rm tot} \int \frac{dn_\gamma}{d\ln x} dx = \frac{f_{\rm th}(\ell_{\rm tot} - \ell_{e,0})}{1 + f_{\rm th}}. \quad (107)$$

7.1. *Heating of the pair gas*

We consider a simple heating model where energy is injected into the pair plasma with the time distribution (76). In this study, we only consider two cases: $\alpha_h = 0$ (constant rate of heating) and $\alpha_h = 1$ (cumulative heat input grows logarithmically with time).

The continuous fashion in which energy is delivered to the pairs is described by the advective term in the F-P equation. The rate of change of the average energy of the pairs due to heating is

$$\frac{1}{2}\frac{dU_{\rm heat}}{dt} = \int \gamma_e\, \partial_p \left[\frac{\gamma_e}{p} A_{\pm,\rm heat} n_\pm(p)\right] dp \quad (108)$$

The factor of 1/2 takes into account that heat is deposited equally into electrons and positrons. From here it is easy to show that

$$A_{\pm,\rm heat} = \frac{1}{2}\left[\left\{\frac{\gamma_e^2}{p} n_\pm(p)\right\}_{p_{\rm min}}^{p_{\rm max}} - n_\pm\right]^{-1} \frac{dU_{\rm heat}}{dt} \quad (109)$$

7.2. *Time evolution of the pair distribution*

As heat is injected into the pair gas, the average energy of the pairs begins to rise. The pairs are also radiatively cooled by Compton scattering soft photons, and very quickly the steady state energy (78) is reached. The

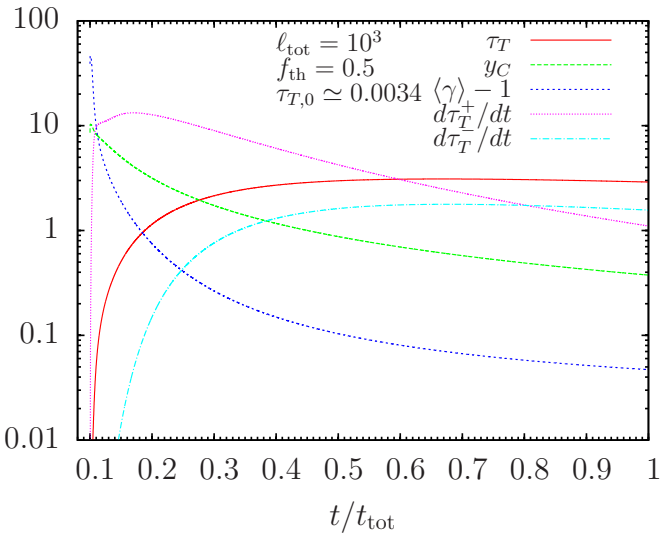

FIG. 5.— State of the pair plasma as a function of time. Total compactness $\ell_{\rm tot} = 10^3$, $f_{\rm th} = 0.5$, and heating profile $\alpha_h = 1$. Initial scattering depth $\tau_{T,0} = 0.0034$ and seed thermal peak energy $x_{\rm pk} = 6 \times 10^{-4}$ correspond to maximum IC photon energy of peak photons $x_{\rm IC,max} = 4\gamma_e^2 x_{\rm pk} = 5$. Plotted quantities: scattering depth (red solid); $y_{\rm C} = (4/3)(\gamma_e^2 - 1)\tau_{\rm T}$ (green dashed); average kinetic energy of pairs (blue wide dot); rates of pair production (purple dot) and annihilation (cyan dot-dashed).

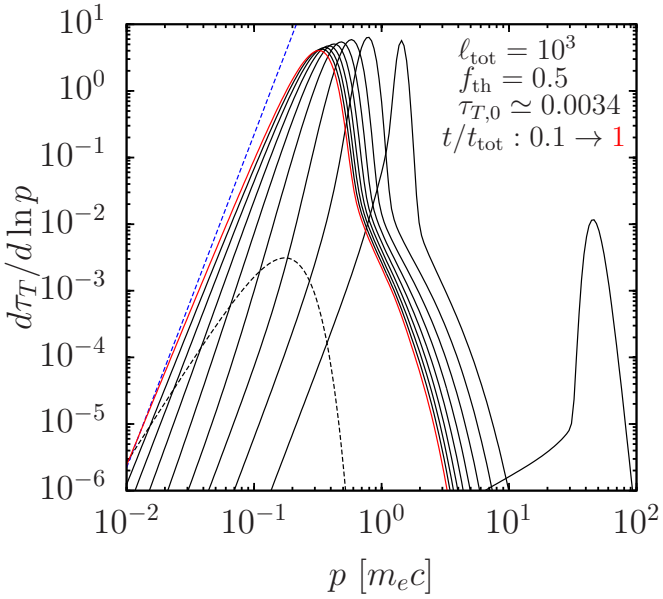

FIG. 6.— Time evolution of the pair distribution in the simulation of Figure 5. Black dashed line: initial distribution, non-relativistic Maxwellian with $\theta_\pm = 0.01$. Solid black curves: evolving particle distribution with peak trending from right to left as the pair density grows. Curves separated by $\Delta t/t_{\rm tot} = 0.1$, starting from $t_0 = 0.1 t_{\rm tot}$. Blue dashed line: $n_\pm(p) \propto p^4$ (see text for details).

maximum energy achieved by the pairs is found by setting $\tau_{\rm T} = \tau_{\rm T,0}$. The equilibrium energy changes adiabatically as soft photons are scattered over the pair creation threshold, as determined by

$$x_1 x_2 \geq \frac{2}{1 - \hat{k}_1 \cdot \hat{k}_2}. \tag{110}$$

Here $\hat{k}_i$ is the unit vector along the wavevector of photon i. The addition of fresh pairs lowers the heating rate per particle.

The evolving state of the pair plasma is shown in Figure 5, for total compactness $\ell_{\rm tot} = 10^3$, $f_{\rm th} = 0.5$, and seed temperature $\theta_\gamma = 2 \times 10^{-4}$. Heating declines as t^{-1} from an initial time $t_0 = 0.1\, t_{\rm tot}$; the initial optical depth $\tau_{\rm T,0} = 0.0034$ corresponds to a mean inverse-Compton energy $\langle x_{\rm IC}\rangle = 4\gamma_e^2\theta_\gamma = 1.6$ for photons drawn from the thermal peak, $x_{\rm pk} = 3\theta_\gamma$, and a maximum $x_{\rm IC,max} = 5$. We recall that for photons of initial energy x_0,

$$x_{\rm IC,max} = 4\gamma_e^2 x_0 \qquad (\gamma_e \gg 1). \tag{111}$$

The optical depth of the pairs continues to rise until the pair annihilation rate,

$$\frac{d\tau_{\rm T}^-}{dt} = \frac{3}{16}\sigma_T c t_{\rm tot} \tau_{\rm T}^2, \tag{112}$$

catches up with the pair production rate. Eventually pair production declines due to a depletion in hard photons, which are no longer generated.

Over the course of the simulation, the pair distribution, shown in Figure 6, remains peaked around some $\langle\gamma_e\rangle$ that is set by the balance between heating and Compton cooling. The Compton cooling rate of high-energy particles is $\propto p^2$, so heating dominates at the low-energy end. When Coulomb collisions are the dominant source of energy exchange between $e^\pm$, their distribution tends to a Maxwellian. Here strong heating and Compton cooling drive the distribution away from complete thermalization, as is evident in Figure 6.

Consider in particular the low-momentum slope of the distribution, which is harder than a Maxwellian. Although Coulomb collisions are most effective at low p, in this case the timescale to establish a thermal distribution is everywhere much longer than that of heating. The low-p slope can be inferred from the continuity equation

$$\frac{d}{dp}\left(\frac{\gamma_e}{p} n_\pm(p) \dot{\gamma}_e\right) = \dot{n}_{\pm,\rm pp}(p) \tag{113}$$

which can be integrated over momentum to give

$$n_\pm(p) = -\dot{\gamma}_e^{-1} \frac{p}{\gamma_e} \int_p^\infty dp\ n_{\pm,\rm pp}(p) \tag{114}$$

Here $\dot{\gamma}_e \propto p^0$ is dominated by the heating term, and we find that $\dot{n}_{\pm,\rm pp} \propto p^2$ at low energies from our numerical simulations. Then equation (114) implies $n_\pm(p) \propto p^4$ at low momenta.

7.3. *Time evolution of the photon spectrum*

We plot the evolution of the photon distribution in the comoving frame of the burst ejecta in Figure 7, in the case $\theta_\gamma \simeq 2 \times 10^{-4}$. The curves correspond to the states of the pairs shown in Figure 6. As the particle energy declines, the Compton upscattered peak shifts to a lower energy until it merges smoothly with the seed thermal peak.

A higher rate of pair annihilation is found in the latter half of the simulation, as the $e^\pm$ become subrelativistic, which results in the formation of an annihilation feature at $x \simeq 1$. A change in spectral slope coincides with the line feature, and is driven by the annihilation of photons of energy exceeding $m_e c^2$ with photons of a lower energy.

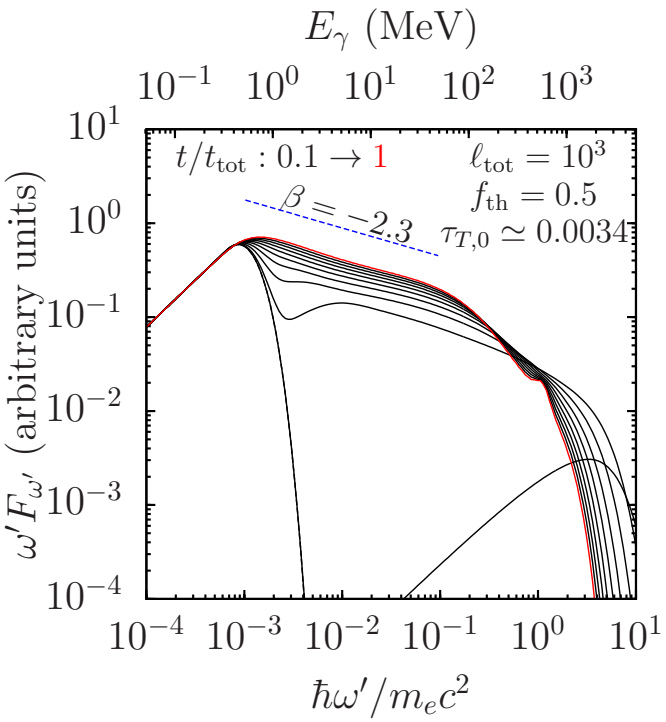
E_γ (MeV)
10^{-1} 10^{0} 10^{1} 10^{2} 10^{3}
$t/t_{\rm tot}: 0.1 \to 1$
$\ell_{\rm tot} = 10^3$
$f_{\rm th} = 0.5$
$\beta = -2.3$
$\tau_{T,0} \simeq 0.0034$
$\omega' F_{\omega'}$ (arbitrary units)
10^{1} 10^{0} 10^{-1} 10^{-2} 10^{-3} 10^{-4}
10^{-4} 10^{-3} 10^{-2} 10^{-1} 10^{0} 10^{1}
$\hbar\omega'/m_e c^2$

FIG. 7.— Time evolution of the photon spectrum in the comoving frame of the burst ejecta for $\ell_{\rm tot} = 10^3$, $f_{\rm th} = 0.5$, $\alpha_h = 1$, and $\tau_0 \simeq 0.0034$. The curves correspond to the state of the photon-pair plasma at different times with $\Delta t/t_{\rm tot} = 0.1$ starting from $t = 0.1 t_{\rm tot}$ with compactness $\ell = \ell_{e,0} + \ell_{\rm th}$. The horizontal axis at the top corresponds to the comoving energy boosted by a factor $\Gamma = 1000$ in the observer's frame. The blue dashed line segment indicates the high energy photon spectral index.

The final comoving photon spectrum looks remarkably like that observed for the majority of GRBs, with a typical low energy photon spectral index $\alpha \sim -1$ below the peak, and high energy index $\beta \sim -2.3$ above it.

7.4. *Dependence on Heating Compactness and Pair Yield*

The spectral index above the peak is largely determined by the ratio $f_{\rm th}$ of the energy in seed thermal photons to that injected in heat (equation (106)). A smooth connection of the spectrum to the peak is obtained for $\ell_{\rm tot} \gtrsim 10^3$, but the efficiency of pair creation drops when $\ell_{\rm tot} \sim 10^2$ to the point that a signficant thermal bump is preserved near the peak.

At this juncture it is worth reviewing where in the outflow strong dissipation will develop due to differential motion of baryons and magnetic field. A net compactness $\ell_{\rm tot} > 10^3$ is easily achieved, according to the following argument.

In the case of a Wolf-Rayet progenitor, baryons derived from the stellar envelope can no longer be accelerated outward by the anisotropic thermal photon pressure when $\ell_{\rm th}$ drops below $\sim 4\times10^3$. Baryon-free parts of the outflow can continue to accelerate outward beyond this point, so that a Lorentz factor differential $\Gamma/\Gamma_{\rm sat,ei} \sim 2$ develops at $\ell_{\rm th} \sim 2^{-4}(4\times10^3) \sim 250$. The corresponding heating compactness is $\ell_{\rm heat} = 500(f_{\rm th}/0.5)^{-1}$, and $\ell_{\rm tot} \gtrsim 10^3$. The electron fraction in the wind emitted by a merged neutron star binary is only $Y_e \sim 0.05 - 0.1$, meaning that the compactness during reheating is 5-10 times larger.

We show the final comoving photon spectrum in Figure 8 for a range of $f_{\rm th}$ and the same total compactness ($\ell_{\rm tot} = 10^3$) as in Figures 5-7. Harder spectra result from larger proportional injections of heat (smaller $f_{\rm th}$). A shift to a constant heating rate ($\alpha_h = 0$) only produces subtle changes in the output spectra. There is more of a difference in the pair yield η_e (the rest energy in pairs created per $m_e c^2$ of injected heat),

$$\eta_e = \frac{d\tau_{\rm T}^{+}/dt}{d\ell_{\rm heat}/dt}. \tag{115}$$

We plot η_e as a function of time in Figure 12 for $f_{\rm th} = 0.5$ and various heating profiles.

We find a strong presence of the thermal bump for $\ell_{\rm tot} = 10^2$ (Figure 10). A glance at the pair yield corresponding to this case reveals insufficient pair production. This, consequently, leads to a higher average kinetic energy of pairs and failure of the high energy spectrum to connect smoothly with the thermal peak.

In Figures 9 and 11, we show the effect on the photon spectrum of increasing the thermal seed photon temperature to $\theta_\gamma = 6\times10^{-4}$, for the same range of compactness and heating profiles. The corresponding results for the pair yield are in Figure 12.

Concentrating the energy injection toward early times ($\alpha_h = 1$) allows a greater number of hard, pair-creating photons to be upscattered before photon collisions raise the pair density and force a drop in particle energy. The net result is a higher pair yield and a higher final optical depth (Figure 13). This also explains the stronger annihilation line as compared with the results of constant heating.

7.5. *Buffering of the Scattering Depth*

Delayed heating in an optically thin outflow preserves a narrow thermal peak that is generated before jet breakout. The rate of pair creation is subject to a regulating effect, due to the inverse relation (78) between inverse-Compton energy and scattering depth. The scattering depth is a function of heating compactness, with lower heating rates generating steeper spectra and lower optical depths (Figure 13).

More generally, the rate of pair creation in a compact and relativistically expanding outflow is sensitive to the mechanism by which high-energy photons are produced. A common starting assumption is that non-thermal electrons (and positrons) are rapidly accelerated, so that radiative cooling follows acceleration. Then a power-law high-energy photon spectrum depends on a power-law distribution of injected particles, such as might originate at a shock. In this picture, the high-energy index (of charged particles or photons) is not connected in a simple or obvious way with the compactness of the outflow. Rapid acceleration of a hard particle distribution of a high compactness would result in large scattering depths, $\tau_{\rm T} \sim \ell^{1/2}$ (e.g. Guilbert et al. 1983).

8. DISTRIBUTED HEATING IN AN EXPANDING MEDIUM

We now combine expansion with continued heating and explore their effect on the comoving photon spectrum. In this situation, radiation interacts with the magnetofluid in a complicated way. The radiation

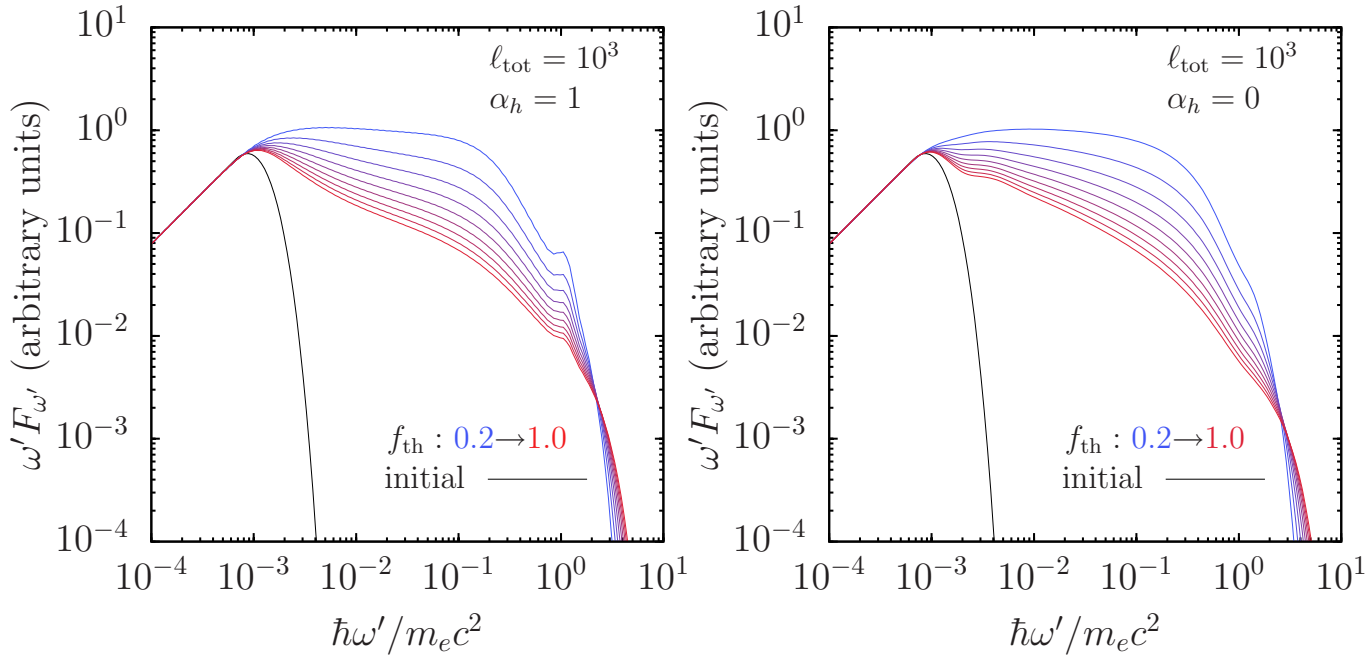

FIG. 8.— Comparison of photon spectra (comoving frame) for total compactness $\ell_{\rm th} + \ell_{\rm heat} = 10^3$ and various relative proportions $f_{\rm th} = \ell_{\rm th}/\ell_{\rm heat}$ of seed thermal energy and added heat. Larger heating rates produce harder spectra. Initial optical depth $\tau_{T,0}$ corresponds to $x_{\rm IC,max} = 5$ for photons draw from the thermal peak. GRB-thermal seed spectrum (equation (97)) with temperature $\theta_\gamma = 2 \times 10^{-4}$. Left panel: $\alpha_h = 1$; right panel: $\alpha_h = 0$.

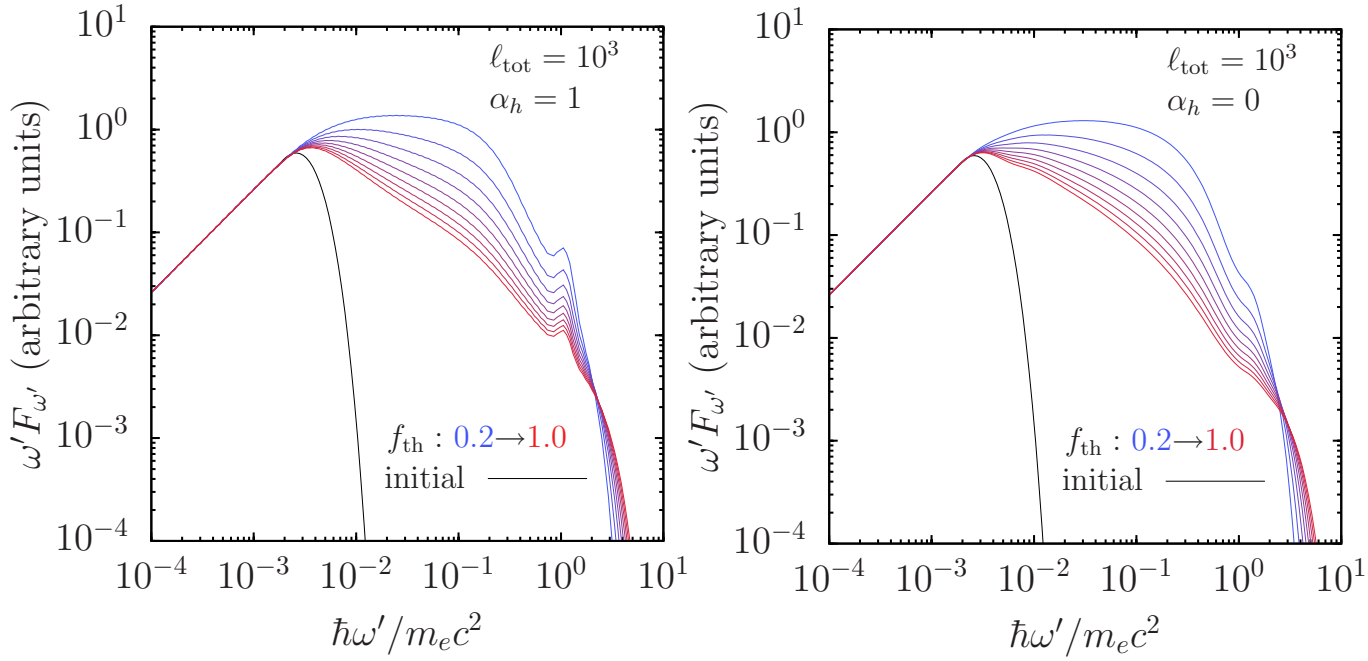

FIG. 9.— Effect of raising seed photon temperature to $\theta_\gamma = 6 \times 10^{-4}$ with $x_{\rm IC,max} = 10$. Other quantities the same as in Figure 8.

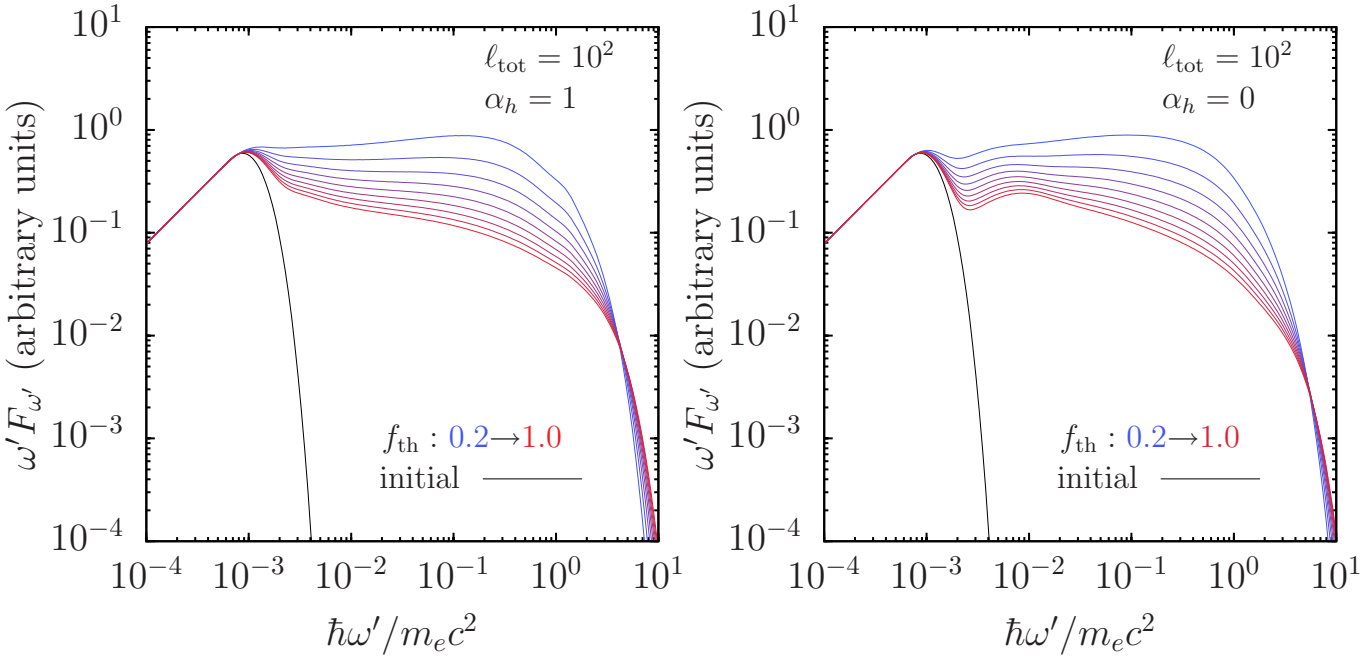

FIG. 10.— Effect on the output spectrum of lowering the total compactness $\ell_{\rm th} + \ell_{\rm heat} = 10^2$. This gives a smaller pair yield (Figure 12), so that the pairs remain trans-relativistic at the end of heating. Now the high-energy tail does not smoothly connect to the peak. Initial optical depth $\tau_{T,0}$ corresponds to $x_{\rm IC,max} = 5$ for photons drawn from the thermal peak.

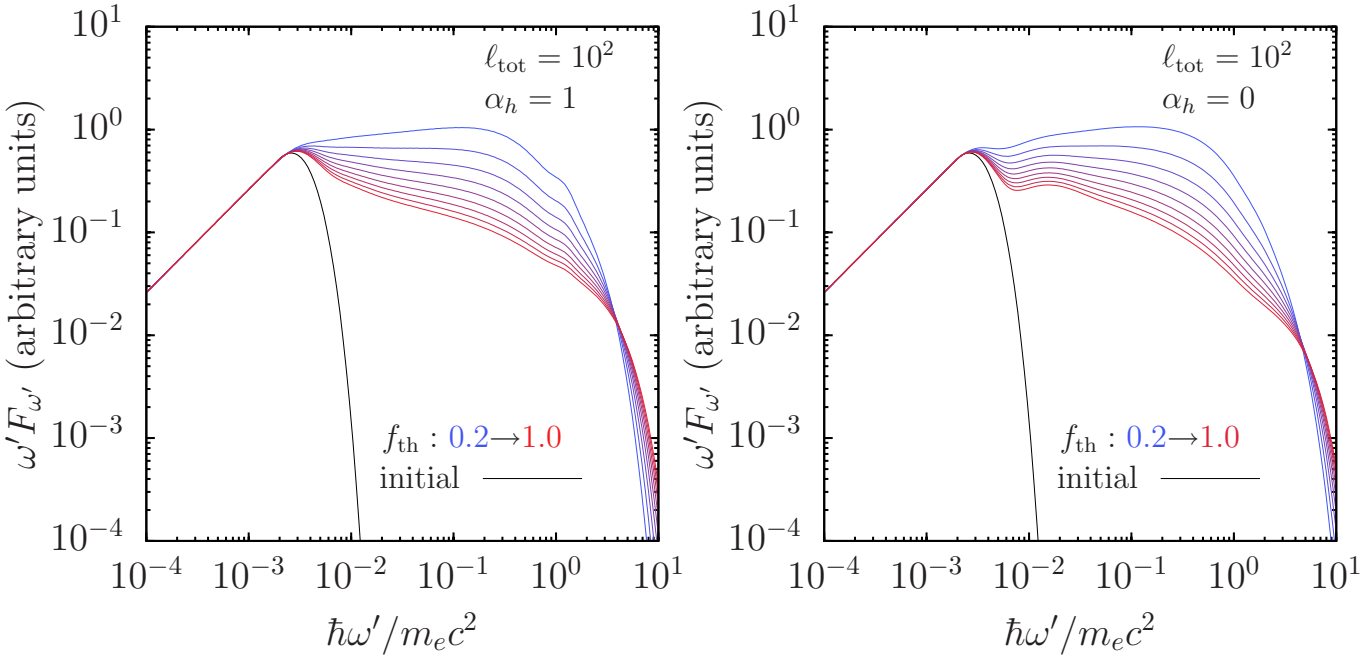

FIG. 11.— Same as Figure 10 but now $\theta_\gamma = 6 \times 10^{-4}$ and $x_{\rm IC,max} = 10$.

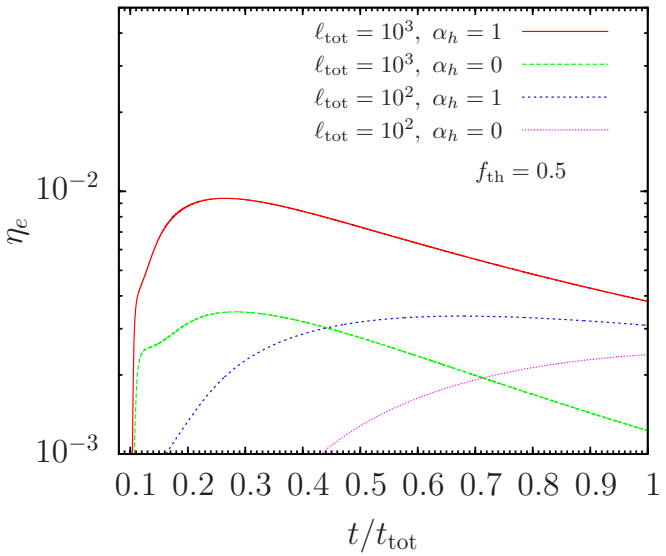
$\ell_{\rm tot} = 10^3,\ \alpha_h = 1$
$\ell_{\rm tot} = 10^3,\ \alpha_h = 0$
$\ell_{\rm tot} = 10^2,\ \alpha_h = 1$
$\ell_{\rm tot} = 10^2,\ \alpha_h = 0$
$f_{\rm th} = 0.5$
η_e
10^{-2}
10^{-3}
0.1 0.2 0.3 0.4 0.5 0.6 0.7 0.8 0.9 1
$t/t_{\rm tot}$

FIG. 12.— Comparison of the pair yield η_e for various heating profiles, and final compactness as plotted in Figures 8 and 10. For all curves $f_{\rm th} = 0.5$. The initial optical depth for $\alpha_h = 1$ ($\alpha_h = 0$) is $\tau_{T,0} \simeq 0.0034$ (0.00087).

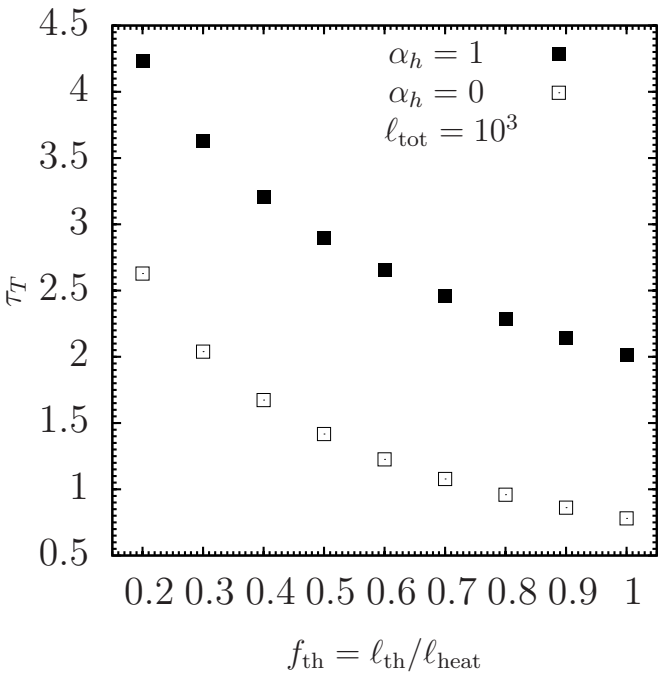

FIG. 13.— Final scattering depth, approximated as Thomson, versus heating compactness. Total compactness (initial thermal + injected heat) $\ell = 10^3$. A flat heating profile also leads to somewhat lower scattering depth.

field transfers energy to or from the expanding magnetofluid, depending on the magnetic field profile (Section 3, Russo & Thompson 2013b). A simplification occurs when $\Gamma \propto r$: then the energy flux of an adiabatically evolved radiation field is preserved in the frame of an external observer, and the differential flow of radiation and matter is minimized (Beloborodov 2011). We focus on this case here.

We let the flow expand by a factor ζ during the heating episode, out to a final radius R_h, Lorentz factor Γ_h, and time t_h. The flow time in the comoving frame relates to the radial extent of the jet through

$$dt = \frac{dr}{\Gamma(r)c} = \left(\frac{R_{\rm h}}{\Gamma_{\rm h} c}\right)\frac{dr}{r}, \tag{116}$$

which gives an exponential expansion, $r(t) \propto e^{\Gamma_{\rm h} ct/R_{\rm h}}$. A rescaled time coordinate is obtained by setting $\hat{t} = 0$ (1) at the start (end) of heating,

$$r(\hat{t}) = \frac{R_h}{\zeta}\exp\left(\ln\zeta\,\hat{t}\right); \quad \hat{t} = 1 + \frac{\Gamma_h c}{R_h \ln\zeta}(t - t_h). \tag{117}$$

The initial time t_0 is found by setting $\hat{t} = 0$.

Adiabatic expansion of a photon gas is governed by the equation

$$\frac{\partial n_\gamma(x)}{\partial t} = \frac{\partial}{\partial x}\left[-\frac{dx}{dt}n_\gamma(x)\right] + \frac{3}{x}\frac{dx}{dt}n_\gamma(x). \tag{118}$$

The energies of individual photons (and all relativistic particles) evolve as $x \propto r^{-1}$, corresponding to

$$\frac{dx}{d\hat{t}} = -x\ln\zeta. \tag{119}$$

The final expansion term in the photon evolution equation (96) is,

$$\dot{n}_{\gamma,\rm exp}(x) = \frac{\partial}{\partial x}[x\ln\zeta\ n_\gamma(x)] - 3\ln\zeta\ n_\gamma(x), \tag{120}$$

and the corresponding term in equation (95) for the pairs is,

$$\dot{n}_{\pm,\rm exp}(p) = \frac{\partial}{\partial p}\left[\frac{\gamma^2}{p}\ln\zeta\ n_\pm(p)\right] - 3\ln\zeta\ n_\pm(p). \tag{121}$$

The corresponding advective coefficients that enter the FP equations are $\{A_\gamma, A_\pm\}_{\rm exp} = \{x\ln\zeta, \gamma\ln\zeta\}$, whereas the dilution of the number density enters the collision-integrals via the terms $\{\dot{n}_\gamma, \dot{n}_\pm\}^{\rm col}_{\rm exp} = \{-3\ln\zeta n_\gamma(x), -3\ln\zeta n_\pm(p)\}$.

Expansion causes a rapid drop in the energy density in radiation,

$$U_\gamma = m_e c^2\int dx\, x n_\gamma(x) \propto r^{-4} \propto \exp\left(-4\ln\zeta\hat{t}\right), \tag{122}$$

corresponding to a net adiabatic dilution ζ^{-4} from the beginning to the end of heating. Since the energy deposited in particles is rapidly transferred to the photons, it is useful to subsume the effects of Compton scattering of the photons in a single heating term,

$$\frac{dU_\gamma}{d\hat{t}} + 4\ln\zeta U_\gamma = \frac{dU_{\rm heat}}{d\hat{t}}. \tag{123}$$

The rate of heat deposition is scaled to the adiabatically evolved thermal energy density,

$$\frac{dU_{\rm heat}}{d\hat{t}} \propto \hat{t}^{-\alpha_h} e^{-4\ln\zeta\hat{t}} U_{\rm th}(t_0). \tag{124}$$

We define a compactness in terms of the adiabatically

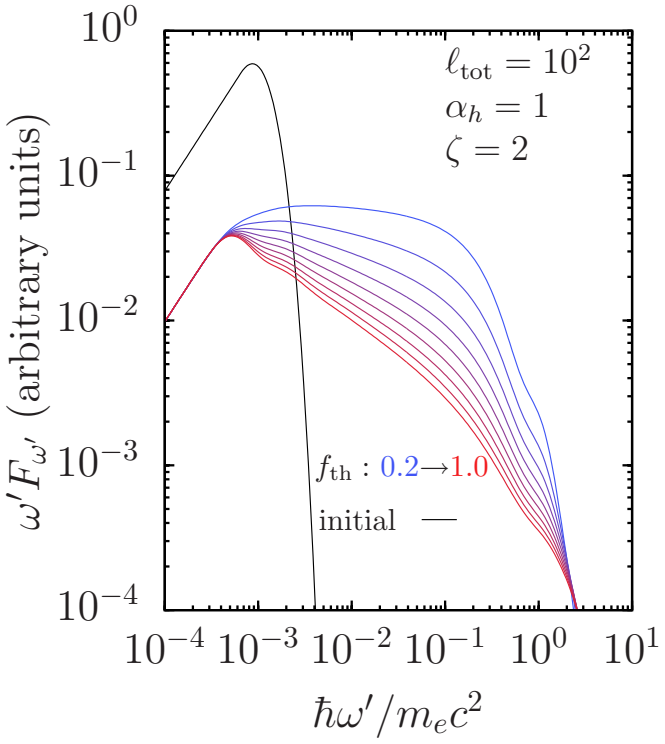

FIG. 14.— Final comoving photon spectra in an expanding medium with final compactness $\ell_{\rm tot} = 10^2$ and a range of $f_{\rm th} = \ell_{\rm th}/\ell_{\rm heat}$. Net expansion factor $\zeta = 2$. The injection of heat follows the profile (124) with a $\hat{t}^{-1}$ envelope ($\alpha_h = 1$) that is cut off at $\hat{t} = 0.1$.

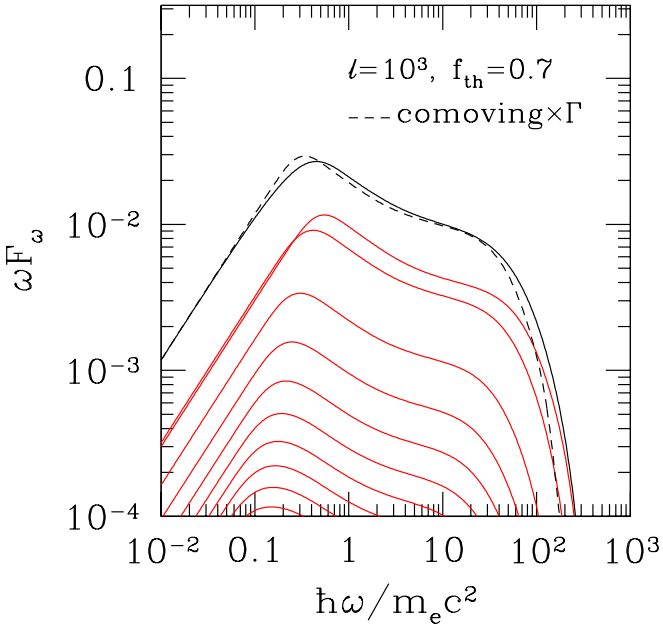

FIG. 15.— Output spectrum (solid black curve) resulting from multiple scattering off a passively expanding pair gas with constant Lorentz factor $\Gamma = 100$ and scattering depth determined by the end of the kinetic calculation of Section 7. Dashed black line: source spectrum, boosted by a factor $\Gamma_0 = 100$ from the comoving one-box calculation, corresponding to $\ell = 10^3$ and $f_{\rm th} = 0.7$. Red curves: time-resolved spectrum, plotted at intervals $\Delta t = 0.5(R_0/2\Gamma_0^2 c)$.

evolved energy density at the end of heating. From

$$U_\gamma(t) = U_{\rm th}(t_0) e^{-4\ln\zeta \hat{t}} + \int_0^{\hat{t}} \frac{dU_{\rm heat}}{d\hat{t}_2} e^{4\ln\zeta(\hat{t}_2 - \hat{t})} d\hat{t}_2, \tag{125}$$

the corresponding thermal and non-thermal compactness are

$$\ell_{\rm th} = \frac{\Gamma_h c}{R_h} \frac{\sigma_T}{m_e c^2} \frac{U_{\rm th}(t_0)}{\zeta^4} \tag{126}$$

and

$$\ell_{\rm heat} = \frac{\sigma_T \Gamma_h}{R_h m_e c} \int_0^1 \frac{dU_{\rm heat}}{d\hat{t}} e^{4\ln\zeta(1-\hat{t})} d\hat{t}. \tag{127}$$

The total compactness can be written in terms of a thermal fraction $f_{\rm th} = \ell_{\rm th}/\ell_{\rm heat}$ as

$$\ell_{\rm tot} = \ell_{\rm heat}(1 + f_{\rm th}). \tag{128}$$

In the case where heat is deposited at a uniform rate ($\alpha_h = 0$), the radiation compactness is

$$\ell_\gamma(\hat{t}) = \ell_{\rm heat}\left(\hat{t} + f_{\rm th}\right) e^{4\ln\zeta(1-\hat{t})}. \tag{129}$$

One observes that the initial thermal compactness can significantly exceed the final compactness with even a modest expansion.

To compare with the static case, we align the final compactness $\ell_{\rm tot}$ and the comoving peak energy in the initial state. Then the peak in the output comoving spectrum shows the effects of adiabatic cooling. The initial optical depth is chosen in a similar way to the calculations of Section 7, so that the maximum inverse Compton energy of photons drawn from the thermal peak is $x_{\rm IC,max} \sim 5$ (equation (111)).

Although the compactness now has a much different time dependence than in the static case, the equilibrium Lorentz factor of the heated pairs depends mainly on the ratio of non-thermal and thermal compactness, and the scattering depth $\tau_{\rm T} \equiv \sigma_T n_e (R_h/\Gamma_h)$,

$$\frac{4}{3}(\gamma_e^2 - 1) = \frac{1}{\tau_{\rm T}\, U_\gamma\, \ln\zeta} \frac{dU_{\rm heat}}{d\hat{t}} - \gamma_e. \tag{130}$$

Adiabatic expansion of the outflow adds an additional cooling term to equation (78), but it has a relatively small effect on γ_e at large ℓ. The contribution of the particles to the initial energy density is very small even after heating to relativistic energies.

Figure (14) shows output spectra corresponding to $\ell_{\rm tot} = 10^2$, with net expansion $\zeta = 2$ and a decaying envelope to the heating rate as defined in equation (124) ($\alpha_h = 1$). The initial compactness, which is closer to $\sim 10^3$, plays a major role in determining the output spectrum: a comparison with Figures 8 and 10 shows a greater similarity with the $\ell = 10^3$ fixed box runs than with the $\ell = 10^2$ case. The effect of adiabatic expansion on the energy of the spectral peak is clearly present.

9. EFFECT OF RESIDUAL SCATTERING ON OUTPUT SPECTRUM

The photon spectra obtained from our static one-box calculations are now evolved by scattering off the frozen, expanding pair gas. We use the Monte Carlo code described in Paper III. Heating is assumed to have turned off, so that the thermal Compton parameter of the pair gas is low, $y_{\rm C} \sim \tau_{\rm T} T_e/m_e c^2 \ll 1$. The spectrum still

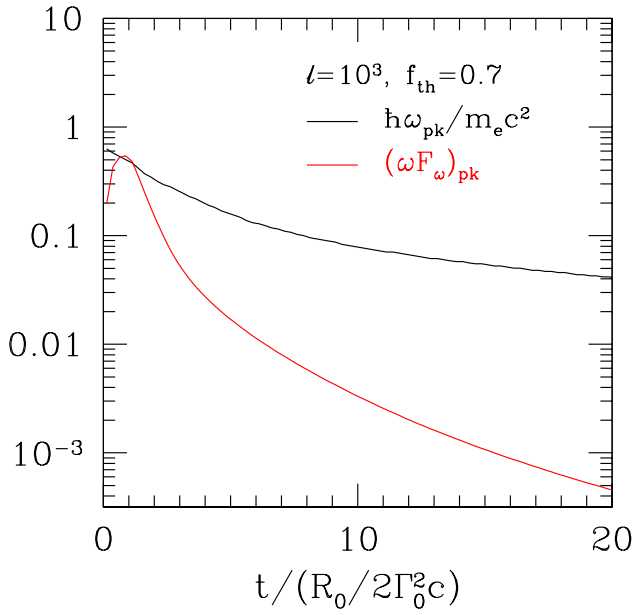

FIG. 16.— Variation with time of spectral peak energy and energy flux at the peak, in a burst based on our one-zone spectral model with $f_{\rm th} = 0.7$, compactness $\ell = 10^3$, and $\Gamma = 10^2$ during the emission of the high-energy tail.

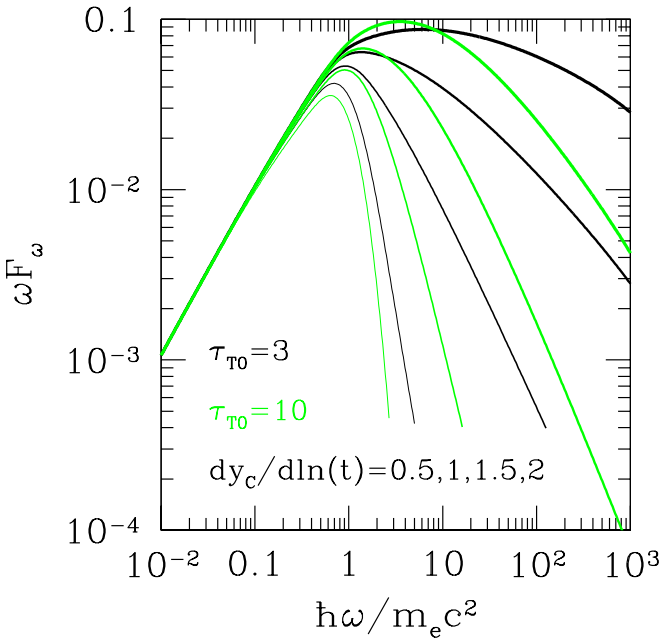

FIG. 17.— High-energy spectrum formed by continuous heating of an outflow that is making a transition from large to small scattering depth, as discussed in the text. Heating starts at a fixed scattering depth (46): $\tau_{T,0} = 3$ (black curves) and $\tau_{T,0} = 10$ (green curves). Compton parameter (131) is $dy_{\rm C}/d\ln t = 2, 1.5, 1, 0.5$ as curves vary to from thickest to thinnest.

evolves, but only modestly, by differential scattering off the bulk flow.

In Figure 15 we compare the output spectrum, averaged over an entire pulse, with the one-box calculation boosted by a factor Γ in energy. The time-resolved spectrum shows little evolution in shape, except for an overall reduction in energy due to side-ways emission. The strong hard-to-soft evolution is shown in Figure 16. This result is characteristic of optically thin and non-thermal emission from curved relativistic shells (Shenoy et al. 2013 and references therein). More details of the pulse evolution are investigated in Paper III.

9.1. *Outflow Heating Continuously from a Large Scattering Depth*

A relativistic outflow that is heated continuously outward from a large scattering depth develops an extended, high-energy spectral tail to a seed thermal radiation field (Giannios 2006; Beloborodov 2010; Lazzati & Begelman 2010). Here we compare the emergent spectrum and hardness evolution with that produced by pair breakdown.

Heating is assumed to continue from inside to outside the photosphere, as in the most recent calculation of Giannios (2008). The outflow starts at a certain initial scattering depth (46) from an initial radius R_0, and the particle energy adjusts so that

$$\frac{4}{3}\left(\langle\gamma_e^2\rangle - 1\right) n_e \sigma_T \frac{r}{2\Gamma^2} = \frac{dy_{\rm C}}{d\ln t} = \text{const.} \qquad (131)$$

We choose a constant Lorentz factor Γ and spherical geometry, and neglect any effect of pair creation or annihilation, as in the previous calculations. Then $n_e(r) \propto r^{-2}$ when $\Gamma \gg 1$.

The output spectrum, as shown in Figure 17, confirms

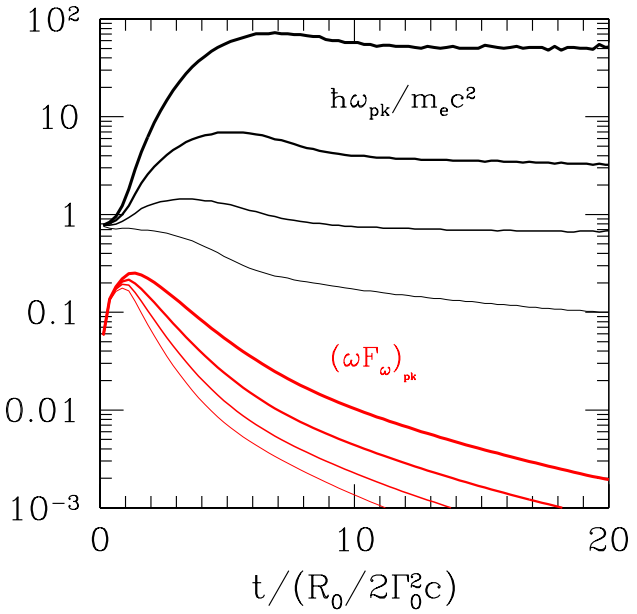

FIG. 18.— Variation with time of spectral peak energy and energy flux at the peak. Spherical, relativistic outflow is continuously heated from inside its photosphere. Curve colors and thickness label $\tau_{T,0}$ and $dy_{\rm C}/d\ln t$ as in Figure 17.

the formation of extended high-energy tail, with an increasing hardness as y_C is raised. However a hard high-energy spectrum is associated with a strong broadening of the spectral peak.

Since harder photons are created by multiple scattering of softer photons, the pulses are broader at high energies, now in strong contradiction with observations (e.g. Fenimore et al. 1995; Norris et al. 1996). For example, the burst shows strong soft-to-hard evolution (Figure 18). Further details of the pulse behavior in this model are discussed in Paper III.

9.2. *Can Multiple Scattering Flatten the Low-energy Spectrum?*

It has been suggested that a relatively hard (e.g. Planckian) source spectrum can, through multiple scattering near a photosphere, be transformed into the flat low-energy spectrum that is characteristically observed in a GRB (e.g. Asano & Mészáros 2013). Different results are obtained by Beloborodov (2010), using a Monte Carlo approach, and Deng & Zhang (2014), using semi-analytic methods. They find that only a modest flattening of the spectrum is possible compared with Rayleigh-Jeans, unless possibly the emission is predominantly off-axis.

Here we revisit this problem in more detail, with the same Monte Carlo approach as above. A spherical shell is assumed, and the low-energy spectral slope is modified by hand. (We use the output of the kinetic calculation with total compactness $\ell = 10^3$ and heating compactness $\ell_{\rm heat} = 2\ell_{\rm th}$ or $f_{\rm th} = 0.5$.)

The output spectrum resulting from a sequence of low-energy spectra ($F_\omega \propto \omega^{1,2}$) is shown in Figure 19. Here the scattering depth has been adjusted upward (to $\tau_{\rm T} = 10$) to accentuate the possible effect of a photosphere. In spite of that, only a slight flattening of the low-energy spectrum is observed. Starting from a Planckian spectrum ($F_\omega \propto \omega^2$) does not lead to anything like a GRB ($F_\omega \sim$ const).

10. DISCUSSION

We have examined the observational imprint of a relativistic, ultraluminous, magnetized outflow emanating from a stellar mass black hole. Such an outflow is naturally produced once the hole is able to acquire an ultrastrong ($\sim 10^{15} - 10^{16}$ G) magnetic field from a massive, orbiting torus. Our focus is on the spectral imprint of delayed dissipation after breakout from a confining medium. We have considered i) acceleration of the magnetized jet following breakout; ii) reheating after it has expanded a factor ~ 100 and the magnetized component has become optically thin to scattering, leading to the creation of a secondary photosphere; iii) the non-thermal spectrum that arises in the simplest case of distributed heating; and iv) differences with the high-energy emission from a photosphere that is continuously heated.

The work presented here, in combination with Russo & Thompson (2013a,b) and Papers I, III, presents a detailed description of the dynamics of GRB outflows and the origin of the extremely bright and variable gamma-ray pulses that are their defining signature.

Energy source for high-energy emission. Differential motion between embedded baryon clouds and the lighter, magnetized jet material produces strong disturbances in the magnetic field once the comoving photon compactness drops below $\ell_{\rm th} \sim 4 \times 10^3 Y_{e\,0.5}^{-1}$. This means that much of the high-energy emission originates in a fairly narrow zone, less than a decade in radius after decoupling between the baryons and the photons.

This differential motion has three features which distinguish it from internal shocks: i) it is actively *driven* within the dissipation zone by the continuing acceleration of the lighter, magnetized jet fluid; ii) it has significant *angular* as well as radial structure; and iii) mod-

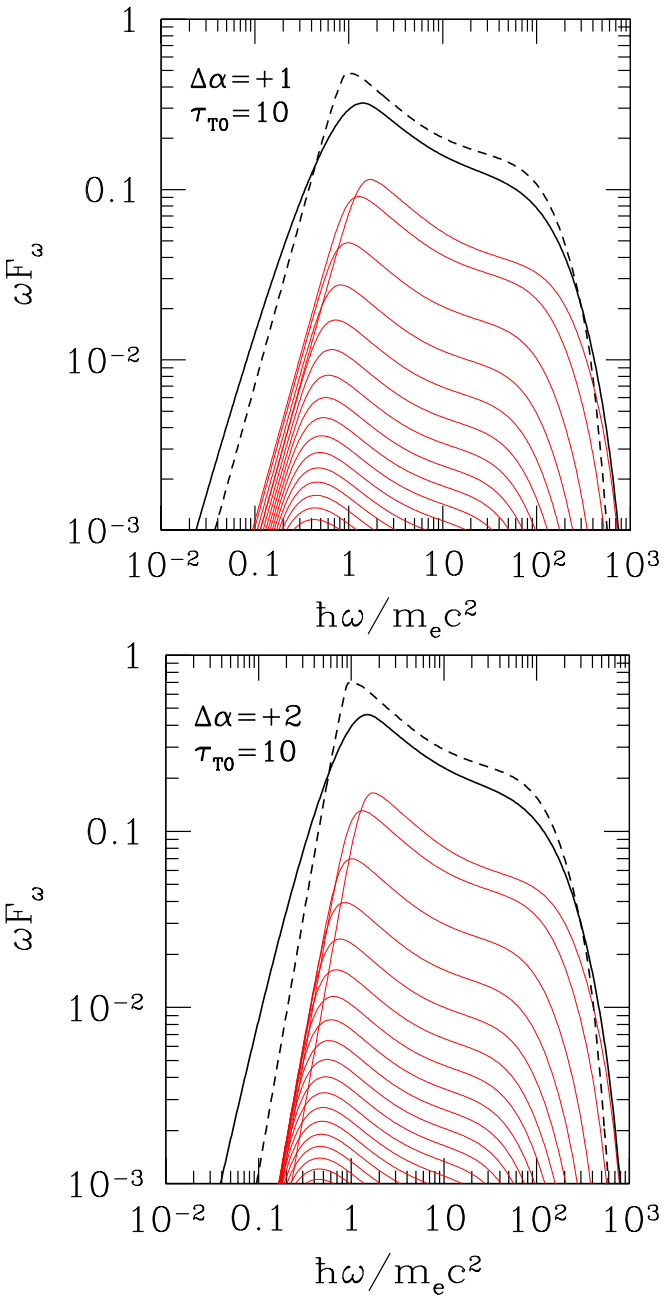

FIG. 19.— Effect of adjusting the input spectrum (dashed black curve, boosted by $\Gamma = 300$) on the output spectrum (solid black curve), processed by Compton scattering off a flow with radial scattering depth τ_{T0} at the injection radius. Top (bottom) panel: $F_\omega \rightarrow (\omega/\omega_{\rm pk})^{\Delta\alpha} F_\omega$ for $\omega < \omega_{\rm pk}$ with $\Delta\alpha = 1$ (2). Red curves: time-resolved spectrum, plotted at intervals $\Delta t = 0.25(R_0/2\Gamma_0^2 c)$.

erately relativistic differential motion is consistent with observed GRB spectra. In the case of internal shocks, high efficiencies demand relativistic collision speeds between shells (Beloborodov 2000), but then the spectrum of accelerated electrons has a relativistic low-energy cutoff, which creates a cooling tail below the spectral peak that is not observed (Ghisellini & Celotti 1999).

Buffering of $\tau_{\rm T}$ during reheating. In strong contrast with emission models involving shock-accelerated particles, the scattering depth is strongly buffered during reheating: as the pair density increases, the energy of the pairs drops, due to a decrease in the heating rate per particle.

Above the spectral peak, harder photons are emitted before softer ones. A high-energy spectral tail, well approximating a power law in many cases, originates from a sequence of relativistic particle states of diminishing mean energy. The highest energy achieved by a Comptonized photon is $\hbar\omega_{\rm IC} \sim \hbar\omega_{\rm pk}/\tau_{\rm T,0}$, where $\tau_{\rm T,0}$ is the radial scattering depth in the magnetized outflow at the onset of re-heating. Within this tail, the highest energy photons are emitted *before* those closer to the seed thermal peak.

Smooth high-energy spectral tail. The tail connects smoothly to the seed thermal peak if the total compactness $\ell_{\rm tot} \gtrsim 10^3$, and if the first photons upscattered during reheating reach an energy $> m_e c^2$ in the comoving frame. For example, a photon index -2.3 above the peak corresponds to a ratio $f_{\rm th} \sim 0.5$ of seed thermal photon energy to injected energy. The minimum thermal compactness is then ~ 300, which lies a factor 10-50 below the critical value $\ell_{\rm th} \sim 4\times 10^3 (Y_e/0.5)^{-1}$ where embedded baryon clouds begin to move differentially with respect to the magnetofluid. By the time the radiation compactness has dropped to this lower value, the differential Lorentz factor has grown to $2-4$ and stronger heating is expected.

The second constraint requires a residual scattering depth $\tau_{\rm T,0} \lesssim 10^{-2}$ in the magnetized jet at the onset of reheating. We show that such a low optical depth is reached by a freely expanding jet by the point that embedded baryons begin to decouple from the radiation field.

Inconsistency between an extended, Comptonizing photosphere and observed GRB pulse behavior. A commonly explored hypothesis is that the high-energy spectrum of a GRB forms in close analogy with an accretion disk corona, by diffusive upscattering of softer thermal photons. We confirm that a high-energy spectral tail can form by such a mechanism, but point out two disagreements with observation: the spectral peak tends to become very broad if the high-energy tail is hard; and, more seriously, the harder photons tend to lag softer ones. We conclude that multiple scattering at a photosphere in a relativistic outflow is not a viable explanation for high-energy spectral tails in GRBs. Residual scattering by the regenerated pairs is found to have a much milder effect on pulse widths.

How rapid is the bulk acceleration of very strongly magnetized jet? A baryon-free jet can reach transparency while still very compact, e.g. $\ell_{\rm P} \sim 10^8$. Then jet material formally has an enormous magnetization, $\sigma \sim \ell_{\rm P}/\tau_{\rm T} \sim \ell_{\rm P}$.

This opens up the possibility that some portion of this material reaches an enormous Lorentz factor in a short time. For example, Granot et al. (2011) showed that a thin, outer layer of a planar magnetofluid expanding into a vacuum reaches a Lorentz factor $\Gamma \sim 2\sigma$ almost instantaneously. Mészáros & Rees (1997) considered the possibility of very high Lorentz factors ($\Gamma > 10^5$) beyond the photosphere of a magnetized jet.

Here we have shown that superposing a modest level of MHD turbulence onto the jet flow, with fractional energy density ε_t in effect limits the magnetization to $\sigma_{\rm eff} \sim 1/\varepsilon_t$. This is demonstrated in an analytic solution to the similarity problem posed by Granot et al. (2011). We also showed that including 'turbulent inertia' in a radiatively forced, transparent jet limits the growth of Lorentz factor to be only slightly faster than linear with radius.

Mapping of temperature at breakout to final spectral peak. We find that the observed spectral peak is the result of three steps. First, as was investigated in Paper I, comptonization by a thermal pair gas with a cyclo-synchrotron source freezes out at a comoving peak energy $\hbar\omega'_{\rm pk} \sim 0.1 m_e c^2$ when the compactness is high (e.g. $\ell \sim 10^7$) but the effective temperature is much less than ~ 20 keV. The output spectrum (97) at this stage is quasi-thermal, with a Wien cutoff above the peak, but a flat spectrum ($F_\omega = $ const) below the peak.

Second, we have argued in Paper III for a modest delay between the emergence of the outflow from the confining medium, and the decoupling of the relativistic magnetofluid from a forward shell of baryonic material. A limited amount of adiabatic softening is possible during this second step, corresponding to a maximum reduction $\sim \mathcal{R}_{\rm br}^{-2/3} \gtrsim 0.2$ in the peak energy. (This softening would be negligible if the magnetofluid continues to be heated during its decoupling from the baryons.) The peak photon energy is preserved after the outflow temporarily becomes transparent.

Third, we have in this paper considered the rescattering of this GRB-thermal spectrum during a delayed pair breakdown that starts at $\tau_{\rm T} \sim 10^{-3} - 10^{-2}$. Here $\omega_{\rm pk}$ increases by a factor ~ 2 as the high-energy spectral tail is generated.

Combining these steps, one finds that the observed peak energy remains within a factor ~ 2 of the seed thermal peak (as seen Lorentz-boosted into the observer's frame). In addition, the formation of individual pulses by a causal process (a corrugation instability of the forward baryon shell) leads to a direct relation between breakout Lorentz factor and opening angle of the outflow, $\Gamma_{\rm br} \sim \delta\theta$. Both of these ingredients are invoked in Paper I to 'derive' the observed relation between $\hbar\omega_{\rm pk}$ and $E_{\gamma,\rm iso}$ (Amati et al. 2002).

10.1. *Outstanding issues*

Maximum range of high-energy spectrum. This is an important test of the emission mechanism, and in principle can be used to distinguish between models in which the source spectrum is a rigid power-law extending above $\sim m_e c^2$ in the comoving frame (e.g. synchrotron radiation by internal shocks), or instead has a break around this energy, as in the mechanism developed here. For example, an outflow producing a burst with $E_{\rm pk} \sim 300$ keV and reaching $\Gamma \sim 300$ in the high-energy emission zone

would, in the second case, have a high-energy spectrum extending to $\sim 10^2$ MeV.

Fermi measurements of GRBs have revealed the onset of extended tails of emission above ~ 100 MeV that appear to be powered by a forward shock (Ackermann et al. 2013). The pulse structure generally simplifies into one or two pulses at these energies, and there is evidence for the emergence of a rising high-energy spectrum during the later stages of the burst (Ackermann et al. 2014, as well as the earlier GRB 941017: González et al. 2003).

In several bright bursts there is a significant deficit in the > 100 MeV emission relative to an upward extension of the high-energy power-law measured near ~ 1 MeV (Guetta et al. 2011). This is generally consistent with our spectral calculations. Suppression of the high-energy emission could also be due to pair conversion if $\Gamma \lesssim 300$ in the prompt emission region, and the emission zone is compact enough.

To decide between these possibilities, an important clue comes from the delay in the onset of the ~ 100 MeV emission, with respect to the $\sim$ MeV band, that is frequently observed (Ackermann et al. 2013). If this delay *and* the deficit in overall > 100 MeV emission were due to pair conversion during the first part of the burst, then the deficits in fluence and duty cycle would be roughly proportional. But, in fact, the > 100 MeV emission is significantly extended in time.

The delayed onset of the hard emission is consistent with expectations based on the pair loading and radiative acceleration of a Wolf-Rayet wind (Thompson 2006). Early on in a burst, the gamma-ray flux across the forward shock is high enough that the wind medium reaches a comparable Lorentz factor to that of the gamma-ray emitting material. The transition from a weak forward shock to a relativistic shock moving into a nearly static medium occurs *during* the prompt phase, leading to the emergence of a high-energy spectral tail with a cooling spectrum $F_\omega \propto \omega^{-1/2}$ (see Sections 3 and 8.2 of Thompson 2006). Detailed calculations of the emergent high-energy spectrum have recently been performed of the interaction between pre-acceleration and high-energy emission including a range of emission channels (Beloborodov et al. 2014) but making a simplifying assumption about the dynamics of the GRB ejecta (that they have already collected into a thin shell that is in dynamical contact with the forward shock).

We conclude that there is evidence for a high-energy spectral tail extending above the peak over a range of $\sim 10^2$, but not necessarily for more extended prompt gamma-ray emission that is not associated with the forward shock. High-energy emission by delayed pair breakdown tentatively passes this test, although more detailed comparisons of different spectral components along the lines of Guetta et al. (2011) are in order.

Particle energy diffusion. Cascading Alfvénic turbulence in a very strongly magnetized pair plasma can become charge starved at a high wavenumber, because wavepackets become very elongated along the background magnetic field. The fluctuating current density $(c/4\pi)k_\perp \delta B$ can exceed the maximum conduction current $n_e e c$ that the ambient pairs can supply. Equating these two quantities, and making use of the wave power spectrum $\delta B(k_\perp)$ fixes the transverse wavenumber $k_\perp^{\rm starve}$. Some recent numerical experiments (Maron & Goldreich 2001; Boldyrev 2006) find $\delta B \sim k_\perp^{-1/4}$, somewhat flatter than the Kolmogorov scaling $\delta B \sim k_\perp^{-1/3}$ that was initially suggested in the theory of strong Alfvénic turbulence developed by Goldreich & Sridhar (1995).

The charge-starvation scale can be compared with the wavenumber $k_\perp \sim \omega_{\rm Pe}/c$ at which Alfvén waves Landau damp on the thermal motion of sub-relativistic pairs. For the adopted wave power-spectrum, this is (Thompson 2006, Paper I)

$$\left(\frac{k_\perp^{\rm starve} c}{\omega_{\rm Pe}}\right)^2 = \frac{\bar\lambda_c}{r/\Gamma}\left(\frac{B}{B_{\rm Q}}\right)^{-8/3}\left(\frac{3\tau_{\rm T}}{2\alpha_{\rm em}}\right)^{5/3}\frac{B^2}{\delta B_0^2}. \quad (132)$$

Here all quantities refer to the comoving frame, δB_0 is the wave amplitude at the outer scale, $\omega_{\rm Pe} = (4\pi n_e e^2/m_e)^{1/2}$ is the plasma frequency, $\bar\lambda_c = \hbar/m_e c$, and $k_{\perp,0} \sim (\delta B_0/B)^{-1}\Gamma/r$ is assumed. Then at breakout at a radius $R_{\rm br} \gtrsim 2\Gamma^2 c t_{\rm eng} \sim 10^{12}$ cm, one finds

$$\left(\frac{k_\perp^{\rm starve} c}{\omega_{\rm Pe}}\right)_{\rm br}^2 = 0.02\,\frac{R_{\rm br,12}^{5/3}(\tau_{\rm T}/3)^{5/3}(\Gamma_{\rm br}/3)^{11/3}}{L_{\rm P\,iso,51}^{4/3}(\delta B/B_0)^2}. \quad (133)$$

One sees that charge starvation can set in at a shallower depth in the cascade than Landau damping. The scattering depth outside breakout in a spherically diverging flow scales as $\tau_{\rm T} \propto r^{-1}\Gamma^2$, hence

$$\left(\frac{k_\perp^{\rm starve} c}{\omega_{\rm Pe}}\right)^2 = \left(\frac{\Gamma}{\Gamma_{\rm br}}\right)^{1/3}\left(\frac{k_\perp^{\rm starve} c}{\omega_{\rm Pe}}\right)_{\rm br}^2 \quad (r > R_{\rm br}). \quad (134)$$

Combining this with equation (133) one see that an Alfvénic cascade still becomes charge starved during the first stages of a delayed pair breakdown, occurring at a Lorentz factor $\sim 10^2\Gamma_{\rm br}$.

It is straightforward to show that the wave energy density $\delta B^2/8\pi$ at $k_\perp \sim k_\perp^{\rm starve}$ is much less than the rest energy density of the background charges, so that its dissipation in one waveperiod is consistent with gradual heating.

More intermittent heating associated with stronger magnetic field gradients remains an interesting possibility, which could be encapsulated in a particle energy diffusivity that is a strong function of energy, e.g. $\mathcal{D} \propto \gamma_e^{2-3}$. This would have the effect of generating a high-energy power-law tail to the particle spectrum, even while the low-energy cutoff remained fixed by a near balance between global heating and cooling. Spectral calculations based on more elaborate models for particle energy diffusion will be explored elsewhere. We are nonetheless encouraged that a high-energy power-law spectrum emerges without invoking such strong particle scattering, by starting from the simplest prescription for uniform, distributed heating.

APPENDIX

A. DETAILS OF THE KINETIC CALCULATIONS

Compton Scattering

In describing Compton scattering, we follow the treatment of Belmont (2009). In particular, we make use of i) the prescription given there for switching from the continuous F-P formalism to a discrete collision integral; and ii) the method for calculating the exact Compton scattering cross-section $d\sigma/dx$ over a wide range of photon and particle energies (see equations (27)-(39) of Belmont 2009). We summarize the approach here for convenience.

Compton scattering can be described exactly as a collision process using the following two collision integrals:

$$\dot{n}^{\rm col}_{\pm,{\rm cs}}(p) = \int dp_0\ n_\pm(p_0) \int_{x_c(p_0)}^{\infty} dx_0\ n_\gamma(x_0)\ c\frac{d\sigma}{dp}(p_0, x_0 \to x(p)) - n_\pm(p) \int_{x_c(p)}^{\infty} dx_0\ n_\gamma(x_0) c\sigma(p, x_0) \tag{A1}$$

$$\dot{n}^{\rm col}_{\gamma,{\rm cs}}(x) = \int dx_0\ n_\gamma(x_0) \int_{p_c(x_0)}^{\infty} dp_0\ n_e(p_0)\ c\frac{d\sigma}{dx}(p_0, x_0 \to x) - n_\gamma(x) \int_{p_c(x)}^{\infty} dp_0\ n_e(p_0)\ c\sigma(p_0, x). \tag{A2}$$

Here $x(p) = x_0 + \gamma_0(p_0) - \gamma(p)$ is obtained from energy conservation. The first and second terms represent scattering into and out of a given energy/momentum bin.

The collision integral cannot be evaluated accurately when $|x - x_0| \ll x_0$: then energy distribution of scattered photons is narrowly peaked around the initial energy, and very high grid resolution is needed to resolve it. A workaround is to Taylor expand the collision integrals to second order over the width of the scattered distribution, which yields F-P equations (98, 99). The advection and diffusion coefficients are obtained by taking moments of the differential cross section,

$$\{A_\gamma(x), D_\gamma(x)\} = \int_0^{p_c(x)} dp\ n_e(p)\ c\sigma_{\{1,2\}}(p, x) \tag{A3}$$

$$\{A_\pm(p), D_\pm(p)\} = \int_0^{x_c(p)} dx\ n_\gamma(x)\ c\sigma_{\{1,2\}}(p, x) \tag{A4}$$

where

$$\sigma(p_0, x_0) = \int dx\ \frac{d\sigma}{dx}(p_0, x_0 \to x) \tag{A5}$$

$$\sigma_1(p_0, x_0) = \int dx\ (x - x_0)\frac{d\sigma}{dx}(p_0, x_0 \to x) \tag{A6}$$

$$\sigma_2(p_0, x_0) = \int dx\ (x - x_0)^2\frac{d\sigma}{dx}(p_0, x_0 \to x) \tag{A7}$$

The limits of integration $x_c(p)$ and $p_c(x)$ depend on the grid resolution, and are shown in Figures 5 and 6 of Belmont (2009) for different resolutions.

Coulomb Scattering

The F-P treatment of Coulomb scattering for arbitrary distribution of particles is developed in the study of Nayakshin & Melia (1998). Here we use the expressions for the diffusion and advection coefficients given in equations (F1)-(F5) of Vurm & Poutanen (2009)

$$A_{\pm,{\rm coul}}(p) = \int dp'\ N_\mp(p') a_{\rm coul}(p, p') \tag{A8}$$

$$D_{\pm,{\rm coul}}(p) = \int dp'\ N_\mp(p') d_{\rm coul}(p, p') \tag{A9}$$

Pair Production and Annihilation

The processes of pair production and annihilation can be exactly described by collision integrals, but their evaluation is typically not limited by grid resolution:

$$\dot{n}^{\rm col}_{\pm,{\rm pp}}(p) = \int dx\ n_\gamma(x) \int dx'\ n_\gamma(x') R_{\gamma\gamma}(x, x' \to p); \tag{A10}$$

$$\dot{n}^{\rm col}_{\pm,{\rm pa}}(p) = -n_\pm(p) \int dp'\ n_\mp(p') R_\pm(p, p'); \tag{A11}$$

$$\dot{n}^{\rm col}_{\gamma,{\rm pa}}(x) = \int dp_+\ n_+(p_+) \int dp_-\ n_-(p_-) R_\pm(p_+, p_- \to x); \tag{A12}$$

$$\dot{n}^{\rm col}_{\gamma,{\rm pp}}(x) = -n_\gamma(x) \int dx'\ n_\gamma(x') R_{\gamma\gamma}(x, x'), \tag{A13}$$

where

$$R_{\gamma\gamma}(x,x') = 2\int dp\ R_{\gamma\gamma}(x,x'\to p); \tag{A14}$$

$$R_{\pm}(p,p') = \frac{1}{2}\int dx\ R_{\pm}(p,p'\to x). \tag{A15}$$

The rate of producing a lepton with momentum p upon the annihilation of two photons with energies x and x', $R_{\gamma\gamma}(x,x'\to p)$, is given in the work of Böttcher & Schlickeiser (1997, equations (24)-(29)). An analytical expression for the rate $R_{\pm}(p,p'\to x)$ of producing a photon with energy x when two leptons of momenta p and p' annihilate each other are provided by Svensson (1982, equations (23), (24), (55)-(58)). The factors of 1/2 (2) account for the fact that two photons are emitted (absorbed) during pair annihilation (creation).

B. DRAG FORCE ON RELATIVISTIC PAIRS HEATED PARALLEL TO **B**.

We now consider the drag force imparted to longitudinally heated electrons and positrons. In addition to non-resonant Compton drag off thermal photons, there is a contribution from cyclo-synchrotron absorption, which we show to be negligible.

In the rest frame of its guiding center, an electron preferentially emits and absorbs soft photons of a similar frequency if the ambient radiation field has a Rayleigh-Jeans slope. After boosting to the lab frame, the absorbed photons then have a characteristic frequency

$$\omega \sim \left[1+\left(\frac{p_\perp}{m_e c}\right)^2\right]\frac{\omega_{\rm ce}}{\gamma_{e\,\parallel}}. \tag{B1}$$

The frequency (B1) does indeed sit in the low-frequency Rayleigh-Jeans tail of the ambient thermal radiation field, and below the flat portion of the spectrum that connects to the spectral peak (Paper I).

Therefore we can define the Rayleigh-Jeans temperature T_c in terms of the pair temperature at breakout, where free-free processes are strong enough to fill in the low-frequency spectrum. Including the adiabatic cooling associated with jet collimation and acceleration outside breakout, one has

$$T_c(r) \sim T_e(R_{\rm br})\left(\frac{r}{R_{\rm br}}\right)^{-1}. \tag{B2}$$

The temperature at breakout is $k_{\rm B}T_e(R_{\rm br}) \sim E_{\rm pk}/3 \sim 0.04\, m_e c^2$, as was found for a magnetized pair plasma of a compactness $\sim 10^4 - 10^6$ (Paper I). Therefore $k_{\rm B}T_c \sim 1$ keV in the reheating zone concentrated at a distance $r \gtrsim 10\, R_{\rm br}$ from the engine.

The drag force that is felt by pairs in relativistic motion along the magnetic field depends on their gyrational energy. A simple close-formed expression for this force is obtained by assuming a two-dimensional thermal distribution with temperature $T_\perp$ in the plane perpendicular to **B**, boosted by a Lorentz factor $\gamma_{e\,\parallel}$ along **B**. As we now derive,

$$\left.\frac{dp_\parallel}{dt}\right|_{\rm synch\ abs} = \frac{5}{2\gamma_{e\,\parallel}}\frac{T_c}{T_\perp}\sigma_T\frac{B^2}{8\pi}. \tag{B3}$$

This drag force is suppressed compared with non-resonant Compton drag off the thermal peak,

$$\frac{dp_\parallel/dt|_{\rm synch\ abs}}{dp_\parallel/dt|_{\rm IC}} = \frac{5}{16\gamma_{e\,\parallel}^3}\frac{T_c}{T_\perp}\left(\frac{T_\perp}{m_e c^2}\right)^{-2}\frac{B^2}{8\pi U_\gamma} \tag{B4}$$

when $k_{\rm B}T_\perp \gg m_e c^2$.

An analogous expression is obtained assuming sub-relativistic gyrations, with most of the absorption at the cyclotron fundamental. Then the ambient photons are aberrated nearly into a direction parallel to **B**, and the corresponding absorption cross section is $\sigma(\omega') = 2\pi^2(e/B)\omega_{\rm ce}\delta(\omega'-\omega_{\rm ce})$. Given the same Rayleigh-Jeans distribution of soft target photons, one obtains

$$\frac{dp_\parallel}{dt} = \frac{dp'_\parallel}{dt'} = \frac{12}{\gamma_{e\,\parallel}}\ln(2\gamma_{\rm e\,\parallel})\left(\frac{T_c}{m_e c^2}\right)\sigma_T\frac{B^2}{8\pi}. \tag{B5}$$

To derive expression (B3), consider a planar distribution of relativistic $e^\pm$ (the sign of the absorbing charge is immaterial) with a temperature $T_\perp \gg m_e c^2/k_{\rm B}$. Superposed on this thermal distribution of gyrations is a uniform motion of the particle guiding centers along **B** at a Lorentz factor $\gamma_{e\,\parallel}$, independent of gyrational energy.

Ambient soft photons of frequency ω and intensity $I_\omega = T_c\omega^2/4\pi^3c^2$ have a frequency $\omega' = \omega/\mathcal{D}$ and intensity $I'_{\omega'} = I_\omega/\mathcal{D}^3$ in the guiding center rest frame, where $\mathcal{D}(\gamma_{e\,\parallel},\mu') = \gamma_{e\,\parallel}(1+\beta_{e\,\parallel}\mu')$ is the Doppler factor. The absorption coefficient in this frame is

$$\alpha'_{\omega'} = \frac{4\pi^3c^2}{T_\perp\omega'^2}\int d\gamma_\perp\frac{\partial^2 P'}{\partial\omega'\partial\Omega'}\frac{dn'_e}{d\gamma_\perp}, \tag{B6}$$

where $\partial^2 P'/\partial\omega'\partial\Omega'$ is the synchrotron power radiated at frequency ω' and direction cosine μ' with respect to $\mathbf{B}$. An electron or positron feels a net force

$$\frac{dp'_\parallel}{dt'} = \frac{1}{n'_e}\int 2\pi d\mu' \int d\omega' (\mu')^2 \alpha'_{\omega'} \frac{I'_{\omega'}}{c} \tag{B7}$$

in the direction of the magnetic field. This force is invariant under the parallel boost, $dp_\parallel/dt = dp'_\parallel/dt'$. After performing the integral over ω', we can substitute

$$\frac{dP'}{d\mu'} = \frac{7}{16}\frac{\gamma_\perp^3 e^4 B^2}{m_e^2 c^3}\left[\frac{1}{(1+\theta'^2\gamma_\perp^2)^{5/2}} + \frac{5}{7}\frac{\theta'^2\gamma_\perp^2}{(1+\theta'^2\gamma_\perp^2)^{7/2}}\right], \tag{B8}$$

with radiation concentrated at an angle $\theta' \simeq \mu' \sim 1/\gamma_\perp$ from the gyrational plane, to obtain equation (B3).

REFERENCES

Abdo, A. A., Ackermann, M., Arimoto, M., et al. 2009, Science, 323, 1688
Ackermann, M., Ajello, M., Asano, K., et al. 2013, ApJS, 209, 11
Ackermann, M., Ajello, M., Asano, K., et al. 2014, Science, 343, 42
Amati, L., Frontera, F., Tavani, M., et al. 2002, A&A, 390, 81
Asano, K., & Mészáros, P. 2013, J. Cosmology Astropart. Phys., 9, 8
Belmont, R. 2009, A&A, 506, 589
Belmont, R., Malzac, J., & Marcowith, A. 2008, A&A, 491, 617
Beloborodov, A. M. 2000, ApJ, 539, L25
Beloborodov, A. M., Stern, B. E., & Svensson, R. 2000, ApJ, 535, 158
Beloborodov, A. M. 2010, MNRAS, 407, 1033
Beloborodov, A. M. 2011, ApJ, 737, 68
Beloborodov, A. M. 2013, ApJ, 764, 157
Beloborodov, A. M., Hascoet, R., & Vurm, I. 2014, ApJ, submitted, arXiv:1307.2663
Blandford, R. D., & Znajek, R. L. 1977, MNRAS, 179, 433
Boldyrev, S. 2006, Physical Review Letters, 96, 115002
Böttcher, M., & Schlickeirser, R. 1997, A&A, 325, 866
Cavallo, G., & Rees, M. J. 1978, MNRAS, 183, 359
Chang, J. S., & Cooper, G. 1970, J. Comp. Phys, 6, 1
Coppi, P. S., & Blandford, R. D. 1990, MNRAS, 245, 453
Daigne, F., & Mochkovitch, R. 1998, MNRAS, 296, 275
Deng, W., & Zhang, B. 2014, ApJ, 785, 112
Dessart, L., Ott, C. D., Burrows, A., Rosswog, S., & Livne, E. 2009, ApJ, 690, 1681
Drenkhahn, G., & Spruit, H. C. 2002, A&A, 391, 1141
Duncan, R. C., Shapiro, S. L., & Wasserman, I. 1986, ApJ, 309, 141
Eichler, D., Livio, M., Piran, T., & Schramm, D. N. 1989, Nature, 340, 126
Eichler, D., & Levinson, A. 2000, ApJ, 529, 146
Fenimore, E. E., in 't Zand, J. J. M., Norris, J. P., Bonnell, J. T., & Nemiroff, R. J. 1995, ApJ, 448, L101
Ghisellini, G., & Celotti, A. 1999, ApJ, 511, L93
Giannios, D. 2006, A&A, 457, 763
Giannios, D. 2008, A&A, 480, 305
Giannios, D., & Spruit, H. C. 2005, A&A, 430, 1
Goldreich, P., & Julian, W. H. 1970, ApJ, 160, 971
Goldreich, P., & Sridhar, S. 1995, ApJ, 438, 763
González, M. M., Dingus, B. L., Kaneko, Y., et al. 2003, Nature, 424, 749
Goodman, J. 1986, ApJ, 308, L47
Granot, J., Komissarov, S. S., & Spitkovsky, A. 2011, MNRAS, 411, 1323
Guetta, D., Pian, E., & Waxman, E. 2011, A&A, 525, A53
Guilbert, P. W., Fabian, A. C., & Rees, M. J. 1983, MNRAS, 205, 593
Jiang, Y.-F., Davis, S. W., & Stone, J. M. 2013, ApJ, 763, 102
Katarzński et al. 2006, A&A, 453, 47
Kobayashi, S., Piran, T., & Sari, R. 1997, ApJ, 490, 92
Lazzati, D., Morsony, B. J., & Begelman, M. C. 2009, ApJ, 700, L47
Lazzati, D., & Begelman, M. C. 2010, ApJ, 725, 1137
Lithwick, Y., & Sari, R. 2001, ApJ, 555, 540
Lightman, A. P., & Zdziarski, A. A. 1987, ApJ, 319, 643
Lyutikov, M., & Blandford, R. 2003, arXiv:astro-ph/0312347
MacFadyen, A. I., & Woosley, S. E. 1999, ApJ, 524, 262
Maron, J., & Goldreich, P. 2001, ApJ, 554, 1175
Matzner, C. D. 2003, MNRAS, 345, 575
McKinney, J. C. 2006, MNRAS, 368, L30
McKinney, J. C., & Uzdensky, D. A. 2012, MNRAS, 419, 573
Mészáros, P., & Rees, M. J. 1997, ApJ, 482, L29
Mészáros, P., & Rees, M. J. 2000, ApJ, 530, 292
Metzger, B. D., Giannios, D., Thompson, T. A., Bucciantini, N., & Quataert, E. 2011, MNRAS, 413, 2031
Nayakshin, S., & Melia, F. 1998, ApJ, 114, 269
Norris, J. P., Nemiroff, R. J., Bonnell, J. T., et al. 1996, ApJ, 459, 393
Paczynski, B. 1986, ApJ, 308, L43
Paczynski, B. 1990, ApJ, 363, 218
Park, B. T., & Petrosian, V. 1996, ApJS, 103, 255
Pe'er, A., & Waxman, E. 2004, ApJ, 613, 448
Pe'er, A., & Waxman, E. 2005, ApJ, 628, 857
Pe'er, A., Mészáros, P., & Rees, M. J. 2006, ApJ, 642, 995
Ramirez-Ruiz, E., Celotti, A., & Rees, M. J. 2002, MNRAS, 337, 1349
Rees, M. J., & Mészáros, P. 1994, ApJ, 430, L93
Rees, M. J., & Mészáros, P. 2005, ApJ, 628, 847
Russo, M., & Thompson, C. 2013, ApJ, 767, 142
Russo, M., & Thompson, C. 2013, ApJ, 773, 99
Sądowski, A., Narayan, R., Penna, R., & Zhu, Y. 2013, MNRAS, 436, 3856
Sari, R., & Piran, T. 1997, ApJ, 485, 270
Shemi, A., & Piran, T. 1990, ApJ, 365, L55
Shenoy, A., Sonbas, E., Dermer, C., et al. 2013, ApJ, 778, 3
Spruit, H. C., Daigne, F., & Drenkhahn, G. 2001, A&A, 369, 694
Stern, B. E., & Poutanen, J. 2004, MNRAS, 352, L35
Svensson, R. 1982, ApJ, 258, 321
Tchekhovskoy, A., Narayan, R., & McKinney, J. C. 2010, 711, 50
Thompson, C. 1994, MNRAS, 270, 480
Thompson, C. 1997, Relativistic Jets in AGNs, ed. M. Sikora & M. Ostrowski, p. 63
Thompson, C. 2006, ApJ, 651, 333
Thompson, C., & Blaes, O. 1998, Phys. Rev. D, 57, 3219
Thompson, C., Mészáros, P., & Rees, M. J. 2007, ApJ, 666, 1012
Thompson, C., & Gill, R. 2014, ApJ, in press (arXiv:1310.2480)
Thompson, C., & Gill, R. 2014, ApJ, submitted
Usov, V. V. 1994, MNRAS, 267, 1035
Vishniac, E. T. 1983, ApJ, 274, 152
Vurm, I., & Poutanen, J. 2009, ApJ, 698, 293
Vurm, I., Lyubarsky, Y., & Piran, T.
Waxman, E., & Mészáros, P. 2003, ApJ, 584, 390
Woosley, S. E. 1993, ApJ, 405, 273
Zalamea, I., & Beloborodov, A. M. 2011, MNRAS, 410, 2302
Zdziarski, A. 1980, AcA, 30, 371
Zhang, B., & Yan, H. 2011, ApJ, 726, 90